UNIVERSITY OF COPENHAGEN
FACULTY OF SCIENCE

Master's thesis

A Study of Top Effective Field Theory at a Future $e^+ e^-$ Collider

Niels Vestergaard

Advisor: Jørgen Beck Hansen

Submitted: May 22 2023

Abstract

This thesis seeks to determine the expected sensitivity to anomalous couplings of $t\bar{t}$ pair production at FCC-ee. The analysis is based on $1.5\,\mathrm{ab}^{-1}$ simulated data at $\sqrt{s} = 365\,\mathrm{GeV}$ in the framework of FCC-ee with the IDEA detector. An event selection is performed to target the search for fully hadronic top quark pairs and a kinematic fit is applied in order to reconstruct the $t\bar{t}$ pair. The 1σ confidence intervals of seven anomalous couplings within top effect field theory are determined separately, based on angular distributions and total cross section.

Acknowledgments

First and foremost I would like to thank my supervisor Jørgen Beck Hansen for his excellent supervision, our many talks and his tireless patience despite my barrage of questions about the project.

I would like to thank my fellow FCC master's students working group at the Niels Bohr Institute for the helpful talks and friendly working environment.

Lastly I would like to thank the the whole experimental particle physics group at the Niels Bohr Institute for the hospitable atmosphere.

Contents

1 Introduction

The field of particle physics continues to stand at the forefront of scientific research, shaping our comprehension of the universe's fundamental constituents and the laws that govern their behavior. The top quark, as the heaviest known fundamental particle has profound significance in the Standard Model and beyond. This thesis focuses on investigating the properties and behavior of top quarks within the context of Standard Model Effective Field (SMEFT) Theory, using simulated data expected from the Future Circular Collider(FCC).

The FCC, a project in planning and development stages at CERN, is set to replace the Large Hadron Collider as the most powerful particle accelerator in the world, giving unparalleled opportunities for research. It is predicted to provide the conditions required to study top quarks with great precision, thereby enabling a comprehensive exploration of this intriguing particle and its interactions.

The unique characteristics of the top quark such as its large mass and short lifetime, make it an excellent probe to test the boundaries of the Standard Model and explore potential new physics.

In this context, the role of Effective Field Theory is to provide a simple framework to capture effects of physics beyond the Standard Model. SMEFT provides a powerful framework to systematically describe new physics without the full machinery of a whole new theory of particle physics.

This thesis will delve into the depths of top quark pair production and hadronic decay at the FCC, within the framework of EFT, with the intention to look for any subtle hints of new physics beyond our current understanding.

In the subsequent chapters, the theoretical groundwork of the Standard Model and Effective Field Theory is outlined. The experimental setup at the FCC is described. An event selection process is described as well as a kinematic fit in order to reconstruct the top quark pairs. Lastly the results are presented showing the effects of anomalous couplings on angular distributions and 1σ confidence intervals are determined for each coupling separately.

2 The Standard Model

The Standard Model of particle physics encompasses our current knowledge of the known fundamental particles and the interactions between them. It can broadly be divided into the matter particles and the bosons. The universe consists of matter particles, fermions, and their interactions are mediated by the bosons. All fermions posses intrinsic angular momentum called spin, equal to $1/2\ \hbar$. The bosons posses a spin of $1\ \hbar$, except for the Higgs boson, which, being a scalar particle, has a spin of $0\ \hbar$.

The matter particles can further be divided into leptons and quarks. The leptons consists of the charged leptons and the neutrinos. They are grouped by their generation, where each charged lepton has a corresponding neutrino.

Similarly the quarks are grouped according to their generation, with each generation having an "up-type" and a "down-type" quark. The up-type quarks (up, charm, top) all posses an electric charge of $2/3\ e$, whereas the down-type quarks (down, strange, bottom) all posses an electric charge of $-1/3\ e$. The complete contents of the Standard Model can be seen in figure 2.1.

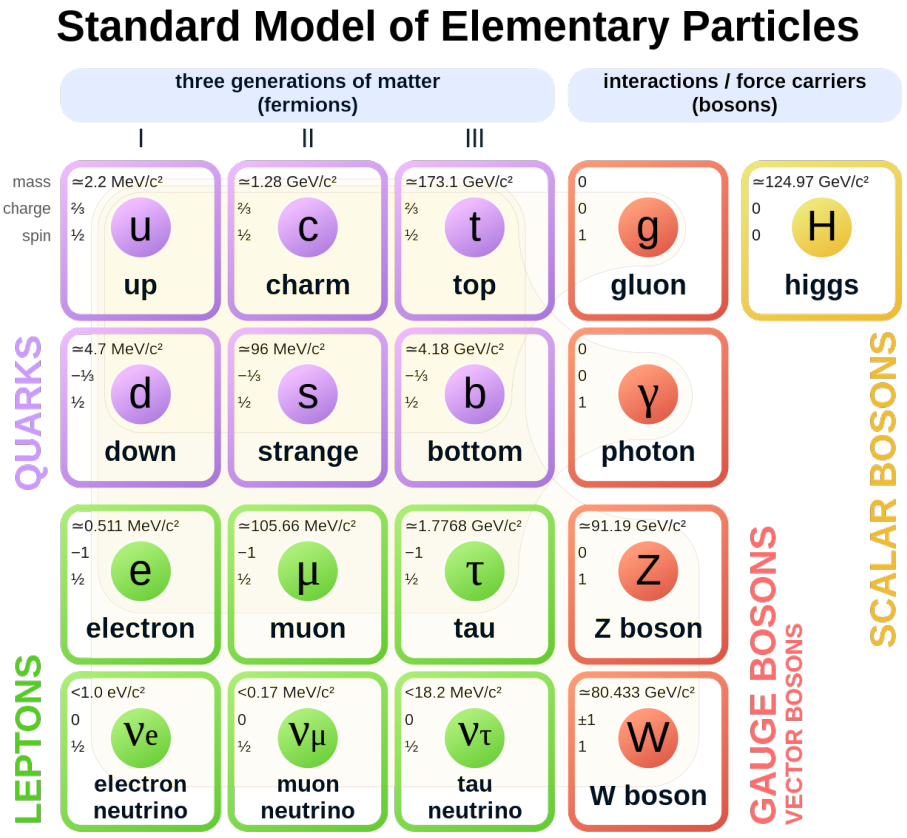

Figure 2.1: The Standard Model of Particle Physics. (Source: Wikimedia Commons)

The Standard Model is formulated in the mathematical language of quantum field

theory. Quantum field theory (QFT) combines principles from quantum mechanics with principles of the special theory of relativity in order to describe the matter particles and forces in a rigorous manner. Among the fundamental quantities in quantum field theory is the *Lagrangian*. The Lagrangian describes the full physics of the Standard Model once the particles and their propertires are defined. The Lagrangian can be written as

$$L = T - V \tag{2.1}$$

where T and V are the kinetic and potential energies of the system, respectively. The Lagrangian $L(q_i, \dot{q}_i)$ can be written as a function of some general coordinates, q_i, and their time derivatives $\dot{q}_i$. The equations of motion can then be determined by the Euler-Lagrange equations

$$\frac{d}{dt}\left(\frac{\partial L}{\partial \dot{q}_i}\right) - \frac{\partial L}{\partial q_i} = 0 \tag{2.2}$$

The concept of the Lagrangian can be extended in order to describe a continuous system by replacing it with the Lagrangian *density* $\mathcal{L}$,

$$L\left(q_i, \frac{dq_i}{dt}\right) \rightarrow \mathcal{L}(\phi_i, \partial_\mu \phi_i) \tag{2.3}$$

Here, the generalized coordinates q_i are instead replaced by fields $\phi_i(t, x, y, z)$ and the time derivatives $\dot{q}_i$ are replaced by the derivatives of the fields

$$\partial_\mu \phi_i = \frac{\partial \phi_i}{\partial x^\mu} \tag{2.4}$$

The fields are continuous functions of some space-time coordinates x^μ, and the Lagrangian L and the Lagrangian density are related by an integral

$$L = \int \mathcal{L}\, d^3\mathbf{x} \tag{2.5}$$

The equivalent of the Euler-Lagrange equation 2.2, can be shown to be

$$\partial_\mu \left(\frac{\partial \mathcal{L}}{\partial(\partial_\mu \phi_i)}\right) - \frac{\partial \mathcal{L}}{\partial \phi_i} = 0 \tag{2.6}$$

In the context of quantum field theory, the term Lagrangian is often used to mean the Lagrangian density. From this point on, the Lagrangian density will simply be identified as the Lagrangian.

2.1 Quantum Electrodynamics

The following descriptions of the different aspects of the Standard Model are based on [1]. Quantum Electrodynamics (QED) is the part of the Standard Model that describes interactions between the electrically charged particles and their interaction mediated by the photon. As such, it can be seen as the quantum field theory description of the electromagnetic interaction. The electromagnetic interaction is required to be invariant under a $U(1)$ local phase transformation. The required local gauge symmetry is expressed as the invariance of the Lagrangian under a local phase transformation of the fields,

$$\psi(x) \rightarrow \psi'(x) = e^{i\alpha(x)}\psi(x) \tag{2.7}$$

The Lagrangian for a free particle can be written as

$$\mathcal{L} = \bar{\psi}(i\gamma^\mu \partial_\mu - m_e)\psi \tag{2.8}$$

As it stands, the free-particle Lagrangian for a Dirac field is not invariant under U(1) local phase transformations. This invariance can be restored by replacing the derivative with a covariant derivative

$$\partial_\mu \rightarrow D_\mu = \partial_\mu - ieA_\mu \tag{2.9}$$

where A_μ is the photon field. With this, the full Lagrangian for QED describing the fields for the electron, the photon and the interactions between them can be written as

$$\mathcal{L}_{\text{QED}} = \bar{\psi}(i\gamma^\mu \partial_\mu - m_e)\psi + e\bar{\psi}\gamma^\mu \psi A_\mu - \frac{1}{4}F_{\mu\nu}F^{\mu\nu} \tag{2.10}$$

where the first term is the kinetic term of a free electron, the second term describes the interaction with the photon field, and the last term describes the kinetic energy of the photon field. The Lagrangian for QED must satisfy a local U(1) gauge symmetry. This second term that describes the interaction between the electron and the photon field is therefore required in order to restore this symmetry. The strength of the QED is described by the fine structure constant α, which can be expressed by the dimensionless term

$$\alpha = \frac{e^2}{4\pi\varepsilon_0 \hbar c} \tag{2.11}$$

This coupling strength is not constant, and varies slowly as a function of the underlying energy scale of the interaction q^2

$$\alpha(q^2) = \frac{\alpha(\mu^2)}{1 - \alpha(\mu^2)\frac{1}{3\pi}\ln\left(\frac{q^2}{\mu^2}\right)} \tag{2.12}$$

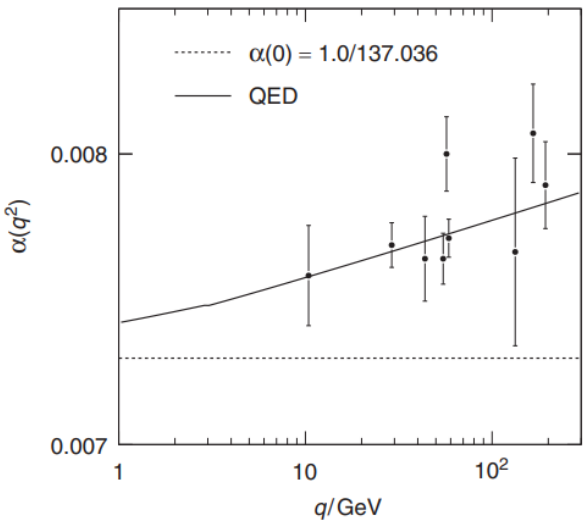

Figure 2.2: Running of α_{EM} as a function energy [1].

Due to the slow change the approximation

$$\alpha(\mu = 0) \approx \frac{1}{137} \tag{2.13}$$

is commonly used in calculations at low energies [1].

2.2 Quantum Chromodynamics

Quantum Chromodynamics (QCD) is the part of the Standard Model that describes interactions between quarks and gluons that posses a color charge. and is mediated by the gluon. As opposed to the single conserved electric charge of QED, the charges of QCD are the three "color" charges

$$r = \begin{pmatrix} 1 \\ 0 \\ 0 \end{pmatrix} \qquad g = \begin{pmatrix} 0 \\ 1 \\ 0 \end{pmatrix} \qquad b = \begin{pmatrix} 0 \\ 0 \\ 1 \end{pmatrix} \tag{2.14}$$

and only particles with non-zero color charge participate in the strong interaction. Similar to the antiparticles of QED having opposite electric charge, antiparticles in QCD have opposite color charge, $\bar{r}$, $\bar{g}$ and $\bar{b}$.

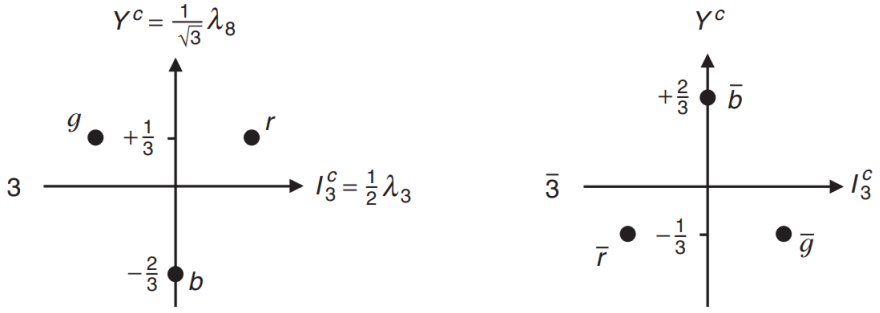

Figure 2.3: Color representation of QCD.

It is also the force responsible for confining quarks inside the proton and the neutron. Whereas QED corresponds to a U(1) local gauge symmetry, the underlying symmetry of QCD is the invariance of SU(3) local phase transformations

$$\psi(x) \rightarrow \psi'(x) = \exp\left[ig_s \boldsymbol{\alpha}(x) \cdot \hat{\boldsymbol{T}}\right] \psi(x) \tag{2.15}$$

where $\hat{\boldsymbol{T}} = \{T^a\}$ are the eight generators of the SU(3) symmetry group, which can be written in terms of the Gell-Man matrices as

$$T^a = \frac{1}{2}\lambda^a \tag{2.16}$$

where $\alpha^a(x)$ are eight functions of some space-time coordinate x. The eight generators of the SU(3) gauge symmetry correspond to the eight massless gluons that mediate the strong interaction. Similar to the running of α in QED, the strength of the QCD coupling is not constant, and it varies as a function of the energy scale of the interaction (q^2). The relationship is given by

$$\alpha_S(q^2) = \frac{\alpha_S(\mu^2)}{1 + B\alpha_S(\mu^2) \ln\left(\frac{q^2}{\mu^2}\right)} \tag{2.17}$$

where B is given by

$$B = \frac{11N_c - 2N_f}{12\pi} \tag{2.18}$$

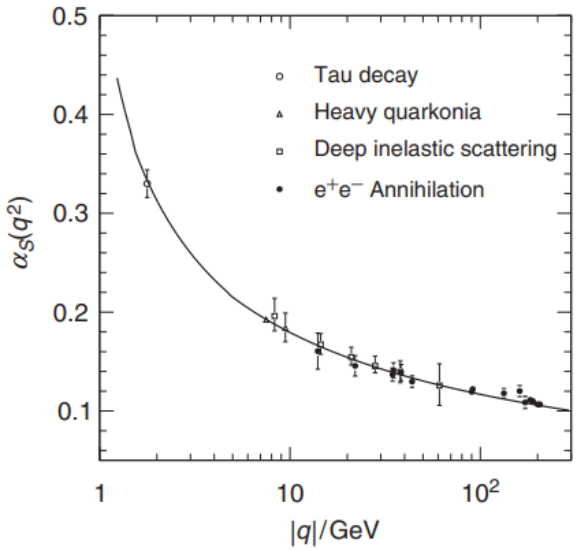

Figure 2.4: Running of α_S as a function energy [1].

where $N_c = 3$ is the number of colors, and $N_f = 6$ is the number of quarks. As $B > 0$ the value of α_S decreases with increasing q^2. At the scale of $|q^2| = m_Z^2$,

$$\alpha_S(m_Z^2) = 0.1184 \pm 0.0007 \tag{2.19}$$

Compared to QED, the running of α_S is much faster. This has profound consequences, as it means perturbation theory cannot be applied at low energy scales, since it requires that the energy scale of the interaction is significantly higher than the underlying scale of α_S. It is therefore only at the relative high energy scale of modern high-energy accelerators that perturbative calculations can be made.

Processes such as $e^+e^- \to q\bar{q}$, the two quarks are initially free and traveling back to back. However due to color confinement, the quarks are observed as jets of colorless particles. This process is known as hadronization. The process happens as the initially free quarks seperate from each other. As the spatial distance increases, the energy stored in the color field increases, analogous to a spring being stretched. When the distance between the quarks is sufficiently large and thus the energy of the color field sufficiently high, new quarks and antiquarks are produced from the energy. This process continues until the energy of all the quarks and antiquarks are low enough to form colorless hadrons. A qualitative depiction of the hadronization process can be seen in 2.5.

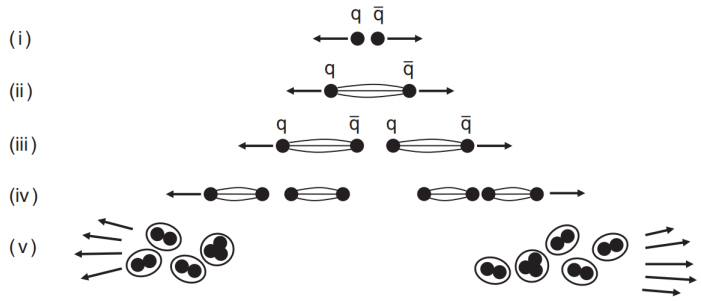

Figure 2.5: Qualitative depiction of the hadronization process [1].

2.3 Weak Interaction

The weak interaction is the third fundamental force described by the Standard Model. The weak interaction differs from QED and QCD in many keys aspects. The *charged-current* weak interaction is mediated by the $W^{\pm}$-bosons and couples fermions together that differ by one unit of electric charge. The charged-current weak interaction is associated with invariance under SU(2) transformations

$$\varphi(x) \rightarrow \varphi^{'}(x) = \exp[ig_W \alpha(\mathbf{x}) \cdot \mathbf{T}\ \varphi(x)] \tag{2.20}$$

where $\mathbf{T}$ are the three generators of the SU(2) group which is given in terms of the Pauli spin matrices as

$$\mathbf{T} = \frac{1}{2}\sigma \tag{2.21}$$

The gauge invariance can only be fulfilled by the introduction of three gauge fields W_{μ}^{k} where $k = 1, 2, 3$ corresponding to three gauge bosons $W^{(1)}$, $W^{(2)}$ and $W^{(3)}$. The physical W-bosons can be identified as the linear combinations

$$W_{\mu}^{\pm} = \frac{1}{\sqrt{2}}\left(W_{\mu}^{(1)} \mp iW_{\mu}^{(2)}\right) \tag{2.22}$$

The last field $W^{(3)}$ will described in the following section. The interaction vertex involving exchanges of the $W^{\pm}$ is of the form

$$\frac{-ig_W}{\sqrt{2}}\frac{1}{2}\gamma^{\mu}(1-\gamma^5) \tag{2.23}$$

where γ^5 is given by

$$\gamma^5 = \begin{pmatrix} 0 & 0 & 1 & 0 \\ 0 & 0 & 0 & 1 \\ 1 & 0 & 0 & 0 \\ 0 & 1 & 0 & 0 \end{pmatrix} \tag{2.24}$$

and g_W is the weak coupling constant. The weak interaction is the only force in the Standard Model that is known to break parity. The violation of parity in weak interactions has far-reaching implications. It introduces a distinction between left and right-handed particles due to the fact that it couples only to left-handed particles and right-handed antiparticles. The strength of the weak interaction is given by the coupling constant a_W

$$\alpha_W = \frac{g_W^2}{4\pi} = \frac{8m_W G_F}{4\sqrt{2}\pi} \approx \frac{1}{30} \tag{2.25}$$

2.4 Electroweak Unification

In the electroweak model the U(1) gauge symmetry associated with QED is replaced by a new $U(1)_\gamma$ gauge symmetry

$$\psi(x) \rightarrow \psi^{'} = \hat{U}(x)\psi(x) = \exp\left[ig^{'}\frac{Y}{2}\zeta(x)\right]\psi(x) \tag{2.26}$$

which gives rise to a new gauge field B_μ that couples to the weak hypercharge Y. The weak hypercharge is the quantum number associated with the electroweak The interaction term has the same form as the interaction term of QED

$$g^{'}\frac{Y}{2}\gamma^\mu B_\mu \psi \tag{2.27}$$

In the electroweak theory, the photon and the Z-boson can be expressed as a linear combination of the B_μ and $W_\mu^{(3)}$ fields.

$$A_\mu = +B_\mu \cos\theta_W + W_\mu^{(3)} \sin\theta_W \tag{2.28}$$

$$Z_\mu = -B_\mu \sin\theta_W + W_\mu^{(3)} \cos\theta_W \tag{2.29}$$

where θ_W is the weak mixing angle. The relationhip between the weak and electromagnetic couplings in term of the weak mixing angle is given by

$$e = g_W \sin\theta_W = g_Z \sin\theta_W \cos\theta_W \tag{2.30}$$

The parameter θ_W is a parameter in the Standard Model with a value of

$$\sin^2\theta_W = 0.23146 \pm 0.00012 \tag{2.31}$$

Another key component of the Standard Model is the Cabibbo–Kobayashi–Maskawa (CKM) matrix. It is a unitary matrix that describes the mixing of quark flavors during weak decays, meaning it explains the probabilities of one type of quark changing into another type. The CKM matrix is given by

$$\begin{pmatrix} d^{'} \\ s^{'} \\ b^{'} \end{pmatrix} = \begin{pmatrix} V_{ud} & V_{us} & V_{ub} \\ V_{cd} & V_{cs} & V_{cb} \\ V_{td} & V_{ts} & V_{tb} \end{pmatrix} \begin{pmatrix} d \\ s \\ b \end{pmatrix} \tag{2.32}$$

The individual elements are found experimentally to be

$$\begin{pmatrix} |V_{ud}| & |V_{us}| & |V_{ub}| \\ |V_{cd}| & |V_{cs}| & |V_{cb}| \\ |V_{td}| & |V_{ts}| & |V_{tb}| \end{pmatrix} \approx \begin{pmatrix} 0.974 & 0.225 & 0.004 \\ 0.225 & 0.973 & 0.041 \\ 0.009 & 0.040 & 0.999 \end{pmatrix} \tag{2.33}$$

In this thesis, the CKM matrix is assumed to be completely diagonal, such that the top quarks always decay such that $t \rightarrow bW$.

2.5 Higgs mechanism

The Higgs mechanism and the associated particle, the Higgs boson, are essential to the Standard Model. It describes the way in which the W and Z bosons and all the fermions acquires their mass. Without the Higgs mechanism, the Standard Model would not be consistent theory, since the masses of the gauge bosons of the electroweak interaction breaks the underlying gauge symmetry. If instead the masses of the fermions were directly in the Lagrangian, it would break the gauge invariance and the Standard Model would not be renormalisable. This problem does not occur in QED and QCD, due to the associated gauge bosons, the photon and the gluons, being massless.

The simplest Higgs model can be described by two complex scalar fields

$$\phi = \begin{pmatrix} \phi^+ \\ \phi^0 \end{pmatrix} = \frac{1}{\sqrt{2}} \begin{pmatrix} \phi_1 + i\phi_2 \\ \phi_3 + i\phi_4 \end{pmatrix} \tag{2.34}$$

The Lagrangian describing this complex scalar field is given by

$$\mathcal{L} = (\partial_\mu \phi)^\dagger (\partial^\mu \phi) - V(\phi) \tag{2.35}$$

with the Higgs potential given by

$$V(\phi) = \mu^2 \phi^\dagger \phi + \lambda (\phi^\dagger \phi)^2 \tag{2.36}$$

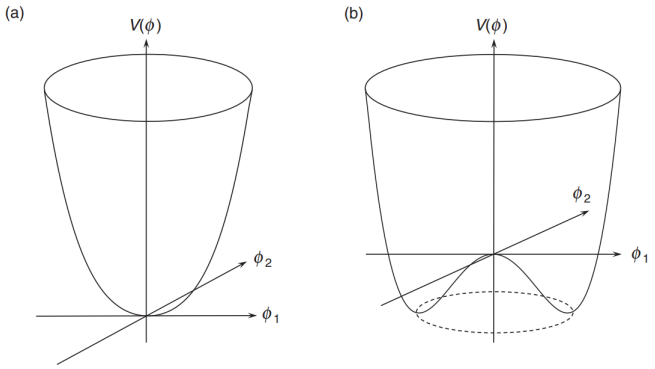

Figure 2.6: The Higgs potential for (a) $\mu^2 > 0$ and (b) $\mu^2 < 0$ [1].

The lowest energy of the field, i.e. the vacuum state obtains non-zero minima

$$\langle 0|\phi|0\rangle = \frac{1}{\sqrt{2}} \begin{pmatrix} 0 \\ v \end{pmatrix} \tag{2.37}$$

where v is the *Vacuum expectation value* (VEV) given by

$$v = \sqrt{\frac{-\mu^2}{\lambda}} \tag{2.38}$$

with a value of

$$v = 246\,\text{GeV} \tag{2.39}$$

The mass of the Higgs boson $m_H = 125\,\text{GeV}$ as well as the masses of the electroweak bosons are all related to the vacuum expectation value

$$m_W = m_Z \cos\theta_W = \frac{1}{2} g_W v \tag{2.40}$$

After the spontaneous symmetry breaking, the Higgs doublet in the unitary gauge can be written as

$$\phi(x) = \frac{1}{\sqrt{2}} \begin{pmatrix} 0 \\ v + h(x) \end{pmatrix} \tag{2.41}$$

The Higgs bosons couples to all fermions in the Standard Model proportional the mass of the fermion

$$m_f = \frac{1}{\sqrt{2}} g_f v \tag{2.42}$$

where g_f is the Yukawa coupling, which determines how strongly a fermion couples to the Higgs field. In the case of the top quark, $g_f \sim 1$, and as such, the top quark is the fermion with the strongest coupling to the Higgs field. This description of the Higgs mechanism concludes the brief description of the Standard Model. A more detailed description can be found in [1].

3 Standard Model Effective Field Theory

Despite the major success of the Standard Model it is not considered to be the final theory of particle physics. An ever increasing amount of experimental data are found to be in incompatible with the core principles of the Standard Model. Among such discoveries are the non-zero mass of neutrinos, the observation of dark matter and the incompatibility with general relativity and as such the inability to combine gravity with the other three forces. In order to probe new physics many theories and approaches are being studied. One such approach is Standard Model Effective Field Theory (SMEFT) and is the approach investigated in this thesis. SMEFT employs a theory-independent approach where the known Standard Model Lagrangian is expanded upon in terms of additional anomalous operators

$$\mathcal{L}_{\text{SMEFT}} = \mathcal{L}_{\text{SM}} + \sum_i \frac{c_i^{(6)}}{\Lambda^2}\mathcal{O}_i^{(6)} + \sum_j \frac{c_j^{(8)}}{\Lambda^4}\mathcal{O}_j^{(8)} + \dots \tag{3.1}$$

where $\mathcal{O}_i$ are the anomalous operators, C_i are coefficients and Λ is the effective energy scale where new physics is expected to arise. The scale of the effective energy parameter is fixed to be 1 TeV in this project. In reality there are thousands of these operators. However it can be shown that all operators of dimension $D = 5$ cannot conserve both baryon and lepton number. Further, operators of higher dimensions are highly suppressed by a factor $1/\Lambda^{D-4}$ and as such their effects will be minimal. The analysis of this project is limited to only non flavor-violating operators. Because of this only operators of dimension $D = 6$ are considered in this thesis.

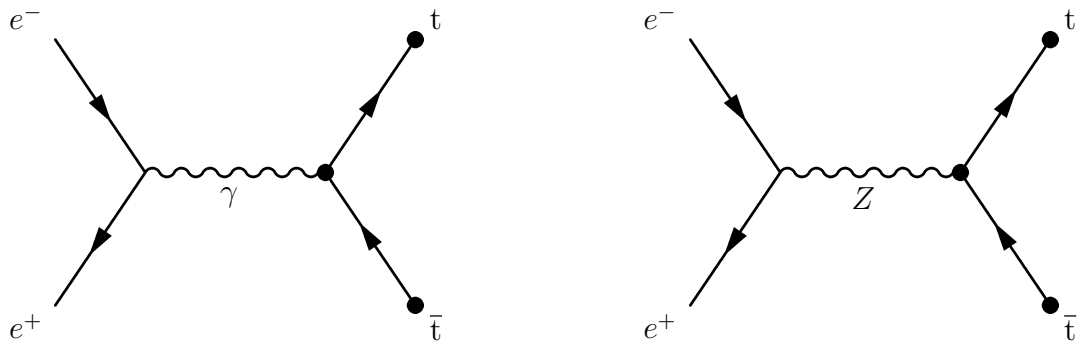

Figure 3.1: Two Feynman diagrams of the process $e^- + e^+ \to t + \bar{t}$. The process can be mediated by a photon (left) or by a Z boson (right).

3.1 Anomalous couplings

In total, there are seven independent operators that affect the $Zt\bar{t}$, $\gamma t\bar{t}$ and Wtb vertices relevant to $t\bar{t}$ pair production being studied. The relevant vertices are shown with black dots in 3.1. Following the notation of [2], these operators can be written as

$$\begin{aligned}
\mathcal{O}_{\phi q}^{(3)} &= i(\phi^\dagger \tau^I D_\mu \phi)(\bar{q}_L \gamma^\mu \tau^I q_L) \\
\mathcal{O}_{\phi q}^{(1)} &= i(\phi^\dagger D_\mu \phi)(\bar{q}_L \gamma^\mu q_L) \\
\mathcal{O}_{\phi\phi} &= i(\tilde{\phi}^\dagger D_\mu \phi)(\bar{t}_R \gamma^\mu b_R) \\
\mathcal{O}_{\phi t} &= i(\phi^\dagger D_\mu \phi)(\bar{t}_R \gamma^\mu t_R) \\
\mathcal{O}_{tW} &= (\bar{q}_L \sigma^{\mu\nu} \tau^I t_R)\tilde{\phi} W_{\mu\nu}^I \\
\mathcal{O}_{bW} &= (\bar{q}_L \sigma^{\mu\nu} \tau^I b_R)\phi W_{\mu\nu}^I \\
\mathcal{O}_{tB\phi} &= (\bar{q}_L \sigma^{\mu\nu} b_R)\tilde{\phi} B_{\mu\nu}
\end{aligned} \tag{3.2}$$

where

$$q_L = \begin{pmatrix} t_L \\ b_L \end{pmatrix}, \quad t_R, \quad b_R \tag{3.3}$$

are the weak interaction eigenstate of the quarks and the covariant derivative, D_μ, is given by

$$D_\mu = \partial_\mu + i g_s \frac{\lambda^a}{2} G_\mu^a + i g \frac{\tau^I}{2} W_\mu^I + i g' Y B_\mu \tag{3.4}$$

where G_μ^a, W_μ^I and B_μ are gauge fields for $SU(3)$, $SU(2)_L$ and $U(1)_L$ respectively, λ^a are the Gell-Mann matrices, τ^I are the Pauli matrices, Y is the weak hypercharge and ϕ is the Higgs doublet.

The total Lagrangian for the Wtb vertex with the Standard Model contribution included is given by

$$\begin{aligned}
\mathcal{L}_{Wtb} = &-\frac{g}{\sqrt{2}} \bar{b} \gamma^\mu (V_L P_L + V_R P_R) t W_\mu^- \\
&- \frac{g}{\sqrt{2}} \bar{b} \frac{i\sigma^{\mu\nu} q_\nu}{M_W} (g_L P_L + g_R P_R) t W_\mu^- + H.c.
\end{aligned} \tag{3.5}$$

where q_ν is the outgoing momentum, g_L, g_R, V_L and V_R are couplings and P_L and P_R are the left- and right-handed chiral projection operators

$$P_L = \frac{1}{2}(1 - \gamma^5) \qquad P_R = \frac{1}{2}(1 + \gamma^5) \tag{3.6}$$

The couplings from the operators of equation 3.2 that contribute are

$$\begin{aligned}
\delta V_L &= C_{\phi q}^{(3)*} \frac{v^2}{\Lambda^2}, & \delta g_L &= \sqrt{2} C_{bW}^* \frac{v^2}{\Lambda^2}, \\
\delta V_R &= \frac{1}{2} C_{\phi\phi} \frac{v^2}{\Lambda^2}, & \delta g_R &= \sqrt{2} C_{tW} \frac{v^2}{\Lambda^2}
\end{aligned} \tag{3.7}$$

Similarly, the total Lagrangian for the Ztt vertex, including the SM contribution, can be written as

$$\begin{aligned}\mathcal{L}_{Ztt} = &-\frac{g}{2c_W}\bar{t}\gamma^\mu(X_{tt}^L P_L + X_{tt}^R P_R - 2s_W^2 Q_t)tZ_\mu \\ &-\frac{g}{2c_W}\bar{t}\frac{i\sigma^{\mu\nu}}{M_Z}(d_V^Z + id_A^Z\gamma_5)tZ_\mu\end{aligned} \tag{3.8}$$

The couplings from the operators that contribute are

$$\delta X_{tt}^L = \text{Re}\left[C_{\phi q}^{(3)} - C_{\phi q}^{(1)}\right]\frac{v^2}{\Lambda^2}, \qquad \delta d_V^Z = \sqrt{2}\ \text{Re}[c_w C_{tW} - sWC_{tB\phi}]\frac{v^2}{\Lambda^2}$$

$$\delta X_{tt}^R = -\text{Re}\ C_{\phi t}\frac{v^2}{\Lambda^2}, \qquad \delta d_A^Z = \sqrt{2}\ \text{Im}[c_W C_{tW} - s_W C_{tB\phi}]\frac{v^2}{\Lambda^2}$$

Lastly, the Lagrangian for the γtt vertex is given by

$$\mathcal{L}_{\gamma tt} = -eQ_t\bar{t}\gamma^\mu A_\mu - e\bar{t}\frac{i\sigma^{\mu\nu}q_\nu}{M_t}(d_V^\gamma + id_A^\gamma\gamma_5)tA_\mu \tag{3.9}$$

The couplings from the operators of equation 3.2 that contribute are

$$\delta d_V^\gamma = \frac{\sqrt{2}}{e}\text{Re}\ [c_W C_{tB\phi} + s_W C_{tW}]\frac{vm_t}{\Lambda^2}$$

$$\delta d_A^\gamma = \frac{\sqrt{2}}{e}\text{Im}\ [c_W C_{tB\phi} + s_W C_{tW}]\frac{vm_t}{\Lambda^2}$$

More detailed description of the operators can be found in [2].

3.2 Effective Matrix Element

The matrix element contains is the quantity that encodes the probability amplitude for a given process to occur. The matrix element is a complex number associated with the transition from one state to another in a quantum system. These states could represent, for example, the initial and final states of a particle interaction. The magnitude squared of this complex number gives the probability for that transition. The matrix element is computed from the Feynman rules that govern the specific particle process. It involves integrating over all possible ways that a given process could occur, each of which is represented by a Feynman diagram. The matrix element incorporates information about the dynamics of the particles involved (via the so-called "propagators") as well as their interactions (via the "vertices" of the Feynman diagrams). Crucially, the matrix element does not include information about the initial and final state kinematics, i.e., the specific directions and energies of the incoming and outgoing particles. This information is instead incorporated into the phase space factor. The product of the matrix element (squared) and the phase space factor gives the differential cross section, which fully describes the likelihood of the process occurring with specific kinematics. The total matrix element can be written as the sum of the Standard Model plus the contribution from the effective operators

$$\mathcal{M} = \mathcal{M}_{\text{SM}} + \mathcal{M}_{\text{EFT}} \tag{3.10}$$

The squared matrix element can then be written as

$$|\mathcal{M}|^2 = |\mathcal{M}_{\mathrm{SM}} + \mathcal{M}_{\mathrm{EFT}}|^2 = |\mathcal{M}_{\mathrm{SM}}|^2 + c_i(\mathcal{M}^*_{\mathrm{SM}}\mathcal{M}_{\mathrm{EFT}} + \mathcal{M}_{\mathrm{SM}}\mathcal{M}^*_{\mathrm{EFT}}) + c_i^2|\mathcal{M}_{\mathrm{EFT}}|^2 \tag{3.11}$$

By inspecting the terms, it can be seen that the total cross section is expected to have a quadratic dependence on an individual coupling. Three points are needed in order to describe a polynomial. For this reason, the simulated event data samples for the anomalous couplings are simulated with a value of ± 1, in order to have three data samples in total, where the last sample is from the Standard Model sample.

4 Experimental Setup

A large aspect of particle physics is experimental in nature. Experimental particle physics involves the design, construction, and implementation of experiments to test predictions and discover new phenomena. A key role of experimental particle physics is to test the predictions of theoretical physics, to either confirm or challenge the existing understanding of fundamental particles and forces. In essence, the two fields of experimental and theoretical particle physics form a symbiotic relationship in the pursuit of expanding the knowledge of the universe. The predictions from theoretical particle physics often guides experimental physics by suggesting what to look for, while the experimental particle physics provides the data needed to confirm or challenge theoretical predictions. When an experimental result aligns with a theoretical prediction, it lends credence to the theory. Conversely, when an experimental result deviates from the theoretical prediction, it can signal the need for a new theory or a modification of the existing one. The analysis of this thesis is based upon the experimental framework of a future particle accelerator and a future particle detector which facilities the experimental study of new physics beyond the Standard Model. In turn, this chapter describes the experimental apparatus of the Future Circular Collider as well as the IDEA detector scheduled to be built.

4.1 Future Circular Collider

The Future Circular Collider (FCC) is a proposed particle accelerator at CERN with the aim of expanding our knowledge of particle physics. It is envisaged to succeed the Large Hadron Collider (LHC) as the flagship particle collider of CERN. The discovery of the Higgs boson at the LHC completed the particle content of the Standard Model. This is however by no means the end. The next step will be precision measurements of the Standard Model, which historically have been used to guide the process of discovery. The project is expected to span a large amount of time, with several years of data taking at different energy regimes. The first stage of FCC will be a lepton collider, which will collide electrons and positrons. Following that, the second stage will be the FCC-hh collider where protons will be collided. This split mode will enable precision measurements of the lepton collider to lead the way to possible areas of discovery, where the much higher energy of the FCC-hh collider has the advantage.

The accelerator itself will be housed in a ~ 91 km ring [3] on the border of France and Switzerland. It was initially proposed to be 100 km but later changed to the current plan of 90.7 km. The construction of such a large and complex underground structure presents significant engineering challenges. The tunnel will need to be precisely aligned to ensure accurate steering of the particle beams, despite geological variations and potential ground movement. It also needs to be deep enough to avoid surface structures and minimize disturbance to the local environment. The construction of the tunnel is expected to start around 2030, and the FCC-ee is expected to start running in the mid 2040's.

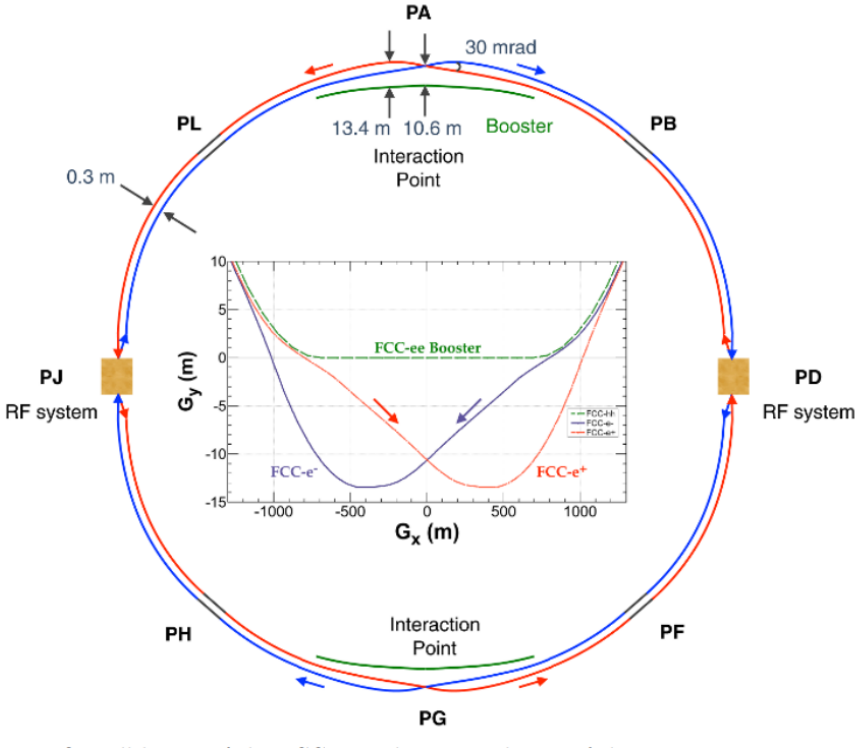

Figure 4.1: Layout of FCC. [4]

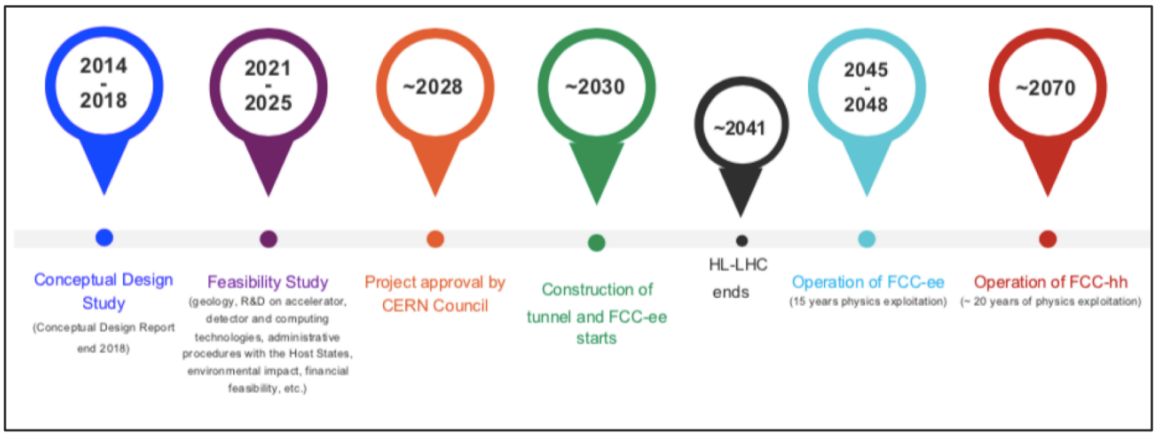

Figure 4.2: Preliminary timeline of FCC operation. [3]

4.2 FCC-ee

The FCC-ee experiment will be the first stage of the FCC project. FCC-ee will be a e+e- collider with the goal of providing excellent precision measurements of the particles and parameters of the Standard Model. The Future Circular Collider Conceptual Design Report describes in detail the goals and motivations as well as technical details about the accelerator and the proposed detectors.

The report states four main research prospects of FCC-ee[4]:

- 1: Measure a comprehensive set of electroweak and Higgs observables with high precision.
- 2: Tightly constrain a large number of the parameters of the standard model.
- 3: Unveil small but significant deviations with respect to the standard model predictions.
- 4: Observe rare new processes or particles, beyond the standard model expectations.

The collider is designed to operate at center of mass energies ranging from 88 to 365 GeV, where the operation points of interest are 91 GeV (Z pole), 160 GeV ($W^{\pm}$ pair production), 240 GeV (ZH production) as well as 340-365 GeV ($t\bar{t}$ production). This is done in order to focus the search by maximizing the number of particles created at each energy point.

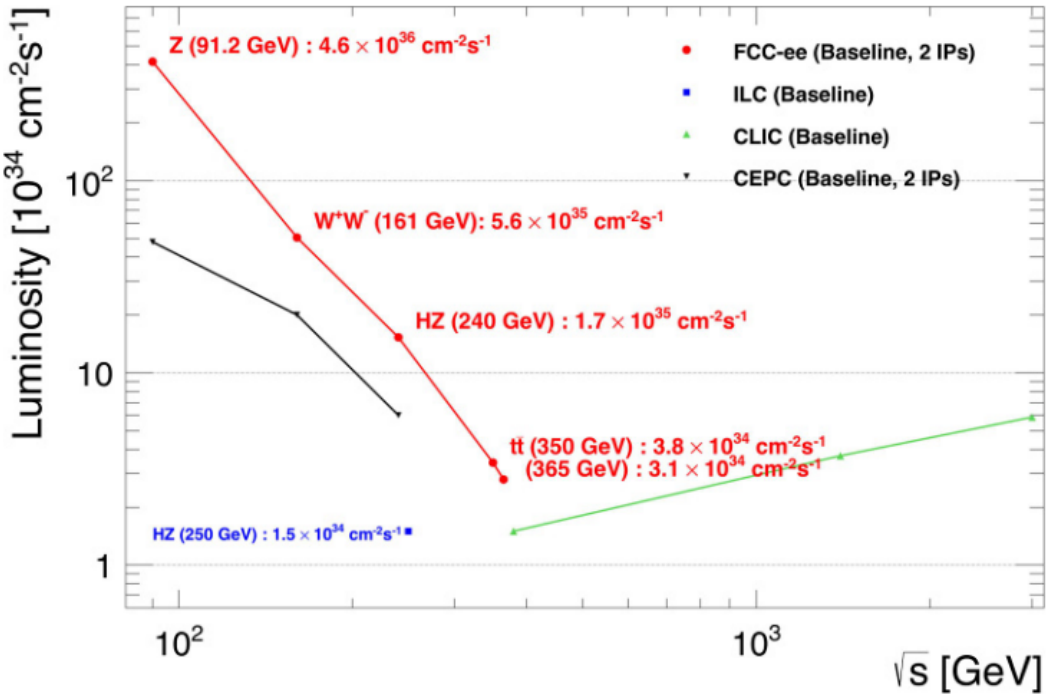

Figure 4.3: Luminosity as a function of energy. [4]

The most important operational parameters are listed in 4.4. [1]

[1]The total integrated luminosity noted here is different than that used for the data analysis. This number is updated one in a while and different sources use different values. This source also states 4 interaction points, whereas the source from which the luminosity is used in the data analysis only states 2 interaction points.

Parameter	Z	WW	H (ZH)	ttbar
beam energy [GeV]	45	80	120	182.5
beam current [mA]	1280	135	26.7	5.0
number bunches/beam	10000	880	248	36
bunch intensity [10^{11}]	2.43	2.91	2.04	2.64
SR energy loss / turn [GeV]	0.0391	0.37	1.869	10.0
total RF voltage 400/800 MHz [GV]	0.120/0	1.0/0	2.08/0	4.0/7.25
long. damping time [turns]	1170	216	64.5	18.5
horizontal beta* [m]	0.1	0.2	0.3	1
vertical beta* [mm]	0.8	1	1	1.6
horizontal geometric emittance [nm]	0.71	2.17	0.64	1.49
vertical geom. emittance [pm]	1.42	4.34	1.29	2.98
horizontal rms IP spot size [μm]	8	21	14	39
vertical rms IP spot size [nm]	34	66	36	69
luminosity per IP [10^{34} $cm^{-2}s^{-1}$]	182	19.4	7.3	1.33
total integrated luminosity / year [ab^{-1}/yr] 4 IPs	87	9.3	3.5	0.65
beam lifetime (rad Bhabha + BS+lattice)	8	18	6	10
	4 years 5 x 10^{12} Z LEP x 10^5	2 years > 10^8 WW LEP x 10^4	3 years 2 x 10^6 H	5 years 2 x 10^6 tt pairs

Figure 4.4: Key parameters of each operational stage of FCC-ee. [3]

As seen from 4.3 and 4.4, the luminosity at the the $t\bar{t}$ energy regime is significantly lower than at the lower energy points. This is due primarily to the synchrotron radiation that is very significant at higher energies. The synchrotron energy is related to the center of mass energy, the radius of the collider and the mass of the particles being accelerated

$$\Delta E \propto \frac{1}{R}\left(\frac{E}{m}\right)^4 \tag{4.1}$$

The low mass of the electron means that the energy loss from synchrotron radiation at each turn becomes a very sizeable effect at higher energies. The energy loss at $\sqrt{s} = 365\,\text{GeV}$ is $10\,\text{GeV}$ per turn. This is not as large of an issue at a hadron collider such as LHC, where the ~ 2000 times heavier protons means the synchrotron radiation is much lower. In order to compensate for radiation losses resulting in the short beam lifetime, top-up injections are used to keep the beam current constant by injecting new electrons and positrons into the beam.

4.3 IDEA detector

The "International Detector for Electron-positron Accelerators" (IDEA) is one of the proposed detectors developed specifically for FCC-ee. The design of the detector consists of a silicon pixel vertex detector, a large-volume extremely-light short-drift wire chamber encased by a layer of silicon micro-strip detectors, a thin and low mass superconducting solenoid coil, a pre-shower detector, a dual-readout calorimeter, capable of independently measuring the electromagnetic and hadronic energy deposits from a particle shower, and a muon chamber within the magnet return yoke.

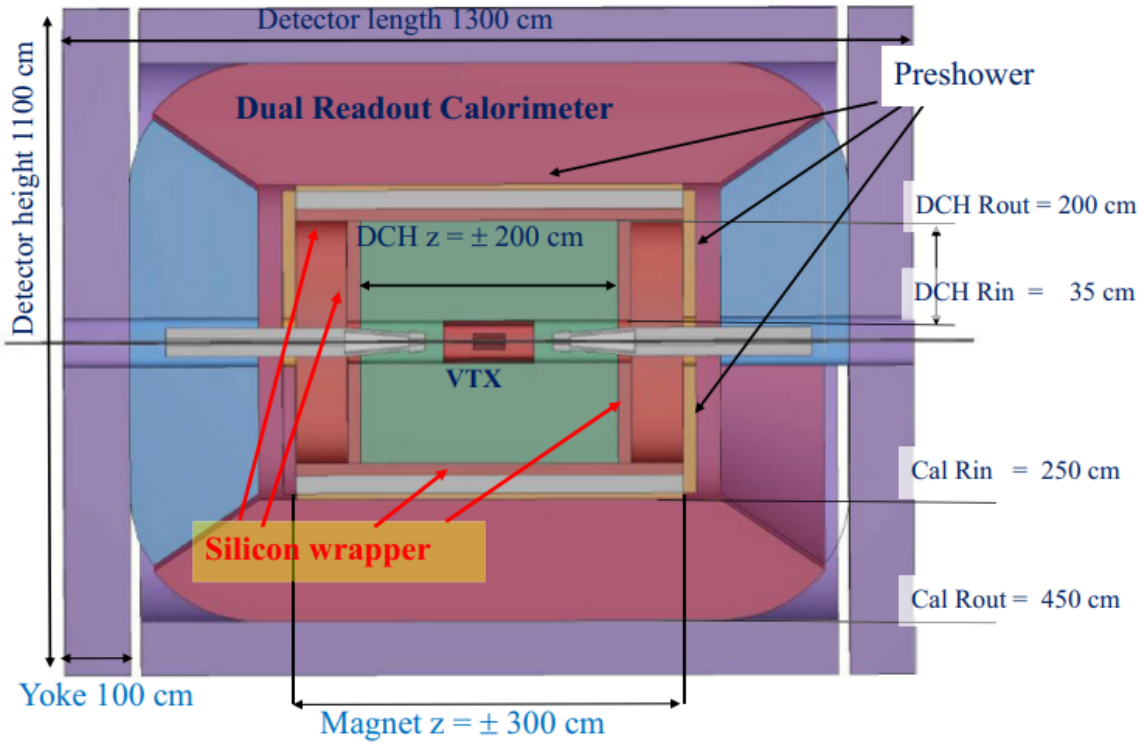

Figure 4.5: Schematic of the IDEA detector [4].

Vertex technology	Silicon
Vertex inner/outer radius	1.7 cm/34 cm
Tracker technology	Drift chamber + silicon wrapper
Tracker half length/outer radius	2.0 m/2.0 m
Solenoid bore radius/half length	2.1 m/3.0 m
Preshower/calorimeter absorber	Lead/lead
Preshower inner/outer radius	2.4 m/2.5 m
DR calorimeter inner/outer radius	2.5 m/4.5 m
Overall height/length	11 m/13 m

Table 4.1: Key parameters of the IDEA detector [4].

The innermost part of the detector, surrounding the beam pipe, is the silicon pixel detector. Test-beam results show an excellent resolution of approximately 5 µm. These very light detectors are the basis for the vertex detector for the IDEA.

The next component in the IDEA detector is the drift chamber (DCH). The DCH is designed to provide good tracking, high-precision momentum measurements as well as providing excellent particle identification. The DCH is co-axial with the 2 T solenoid field and extends from an inner radius of $R_{in} = 0.35\,\text{m}$ to an outer radius of $R_{out} = 2\,\text{m}$ for total length of $L = 4\,\text{m}$. It consists of 112 co-axial layers arranged in 24 sectors. The sizes of the cells size vary between 12.0 mm and 14.5 mm for a total of 56448 drift cells. The spatial resolution of the tracking system is expected to be $\sigma(1/p_T) \simeq a \bigoplus b/p_T$ where $a \simeq 3 \cdot 10^{-5}$ GeV^{-1} and $b \simeq 0.6 \cdot 10^{-3}$.

The preshower detector is placed between the magnet and the calorimeter in the barrel region, and between the drift chamber and the end-cap calorimeter in the forward region. The preshower detector further improves the tracking resolutions as well as tagging pions by tagging both photons from their decay.

The dual-readout calorimeter made of lead fibers surrounds the second preshower layer. The calorimeter will have an excellent energy resolution for both electromagnetic and hadron showers as a result of both being sensitive to the independent signals from scintillation light as well as Cerenkov radiation. The resulting energy resolution by combing the two signals are estimated from preliminary simulations to be $10\%/\sqrt{E}$ for isolated electrons and $30\%/\sqrt{E}$ for isolated pions. The calorimeter further provides very good intrinsic discrimination between muons, electrons/photons and hadrons assuming the measured particles are isolated with a 98% efficiency for separating electrons and protons. In addition to the particle identification capabilities, the high degree of transverse granularity allows for the separation of close showers. Several ways to implement methods of disentangling the signals produced by overlapping electromagnetic and hadron showers are currently being investigated.

4.4 Simulation and Reconstruction Framework

The analysis in this thesis is based on simulated data. The simulation tools used are all contained within the Future Circular Collider Software **FCCSW** [5] framework . The framework itself consists of multiple components that facilitate the entire process of simulating Monte Carlo events and the subsequent steps of hadronisation, detector response and data analysis. The central components are **Pythia** [6], **Delphes** [7] and **EDM4HEP** [8]. Pythia is a general purpose Monte Carlo event generator, that facilitates the generation of high-energy collision events. This includes both the hard interaction of a particular particle process, as well as decay and subsequent fragmentation of final state partons. EDM4hep is a generic event data model for future colliders where the structure of the output file is given. Pythia is used in conjunction with Delphes, which is a software package that facilitates fast detector response simulation. In order to perform a simulation with Pythia and Delphes, the command "DelphesPythia8_EDM4HEP" is called along with a Pythia command file and a Delphes card. The Pythia command file instructs the program which hard process to simulate and the Delphes card holds the specifications of the particle detector to simulate. The analysis of this project is based on the capabilities of the IDEA detector. Therefore, the Delphes detector card used is that of the IDEA detector. This means that all the specifications and geometrical details of the IDEA detector are encoded into the "IDEA.tcl" file that is called in conjunction with the "DelphesPythia8_EDM4HEP" command. This includes numerous effects such as the calorimeter resolutions, the magnetic fields used for measurements of charged particles etc. The output is a **ROOT** file [9]. ROOT is the industry standard when it comes to particle physics analysis. It is a an open-source data analysis framework developed at CERN specifically for analyzing large amounts of data. It also provides a number of helpful functionalities such as statistical analysis as well as easy-to-use data visualization.

4.4.1 Reconstruction object definitions

The purpose of Delphes is to provide the detector response to the simulated event processes. Delphes reconstructs simulated particles based on the specifications of the specific detector used. In Delphes, an "object" refers to a reconstructed particle or jet. Some of the object types that Delphes can handle include:

- Electrons: Identified by their characteristic signature in the detector's electromagnetic calorimeter.
- Muons: Identified by their penetration through multiple detector layers.
- Jets: These are "clusters" of particles produced by quark or gluon fragmentation.
- Missing transverse energy: This is not a directly observable object but is inferred from the imbalance of the total energy in an event.

Each of these object types has an associated "definition" in Delphes, which includes the algorithm used to identify and reconstruct the object from the raw simulated detector data, as well as any cuts or criteria applied to the reconstructed objects. For example, an electron might be identified by a cluster in the electromagnetic calorimeter with a matching track, and the electron definition might include a minimum transverse momentum or a maximum pseudorapidity.

4.4.2 Jet reconstruction

As a result of the hadronization process, jets of particles are measured inside the detector instead of individual quarks. These jets appear as a cone-shaped cascade of of collimated particles. The reconstruction of the jets is in general not a trivial task, and the definition of a jet is not unique. The type of particle accelerator is also an important consideration when choosing a jet algorithm. Hadron colliders such as LHC produce an immense amount of background, therefore any jet algorithm used must be able to handle said background. In the clean environment of a lepton collider such as FCC-ee, this is a much smaller issue. Nevertheless, the choice of jet algorithm is an essential aspect of the analysis. In general jet algorithms work in a iterative

manner. Firstly, the jet algorithm classifies the reconstructed particles as *pseudojets*. Pseudojets collections of particles that are clustered together and treated as a single object. At each iteration the jet algorithm combines the pseudojets based on the distance measure that is unique to each jet algorithm. The pseudojets closest based on the distance measure are then combined. This iterative process is continued until some cut-off value has been reached. Along with a definition of distance measure, a jet algorithm is used with a recombination scheme. The recombination scheme determines *how* the jets are to be combined once the minimum of the distance measure has been found. Three of the main jet combinations schemes used in lepton colliders are E-scheme, the $E0$-scheme and the p- scheme. Firstly, the E-scheme is defined such that pseudojet i and j are replaced by a pseudojet k with four-momentum

$$\mathbf{p}_k = \mathbf{p}_i + \mathbf{p}_j \tag{4.2}$$

The advantages of this particular scheme is that it is Lorentz invariant by construction, such that it automatically conserves energy and momentum. The disadvantage is that

it introduces a non-zero mass for the jet that cannot be accounted for in full [10]. Conversely, for the $E0$-scheme, the pseudojet k is rescaled such that is has 0 invariant mass

$$E_k = E_i + E_j, \qquad \vec{p}_k = \frac{E_k}{|\vec{p}_i + \vec{p}_j|} \cdot (\vec{p}_i + \vec{p}_j) \tag{4.3}$$

This recombination scheme is not Lorentz invariant since only the energy is conserved. Therefore it can only be applied in the laboratory frame. Lastly in the p-scheme the four-momentum is rescaled in order to have 0 invariant mass

$$\vec{p}_k = \vec{p}_i + \vec{p}_j, \qquad E_k = |\vec{p}_k| \tag{4.4}$$

In this thesis, the *Durham* algorithm is used along with the E-scheme. In the Durham algorithm, the distance measure is defined as

$$d_{ij} = min(E_i^2, E_j^2)(1 - \cos\theta_{ij}) \tag{4.5}$$

It incorporates both information about the energy as well as angular information to combine jets. This choice was made on the basis of the work of [11], where the Durham algorithm was found to be among the best performing algorithms when it came to uniquely matching quarks at the Monte Carlo truth level to the reconstructed jets. The Durham algorithm also performed the best at separating the decay products of the b-quark into the same jet. The specific properties of the b-quark makes it possible to distinguish jets originating from b-quarks from other types of hadronic jets. The efficiency of the b-tagging in this analysis is set to be 80% in order to not overestimate the real efficiency that will be possible at FCC. It could be envisioned that this could be improved for example by implementing machine learning techniques.

The jet algorithm is implemented with **FastJet** [12]. FastJet is a software package that provides fast native implementations of many sequential recombination algorithms. In this analysis, FastJet is used in the exclusive clustering mode, meaning that a predefined number of jets is defined, and the jet algorithm concludes whenever that specific number of jets has been reached.

5 Monte Carlo Simulation Samples

This section describes the Monte Carlo data samples as well as the relevant backgrounds and the simulation of event samples of anomalous couplings that the analysis of this project is based upon.

5.1 Hadronic $t\bar{t}$ Production

In this thesis, the process of interest is a pair of top quarks in the fully hadronic decay mode

$$e^+e^- \to t\bar{t} \to bW^+\bar{b}W^-, \quad W^+ \to q_\ell\bar{q}_\ell, \quad W^- \to q_\ell\bar{q}_\ell \tag{5.1}$$

This particular decay channel has a number of advantages and disadvantages when it comes to looking for new physics. The main advantages is the relatively high branching ratio of the W-bosons. With a hadronic branching ratio of 45.44% [13], it is the most common decay channel of the $t\bar{t}$ pair. This in turn translates to a large amount of statistics and therefore improving the possibility of discovery. However, the fully hadronic decay mode also has its drawbacks. Hadronic jets are in general not measured as well as leptons. Further, the many jets in the final state increases the chances of a jet partially of fully escaping detection by flying out near the beam pipe. By contrast, the fully leptonic $t\bar{t}$ event has a relatively low branching ratio, but increased resolution and easier reconstruction. The semi-leptonic $t\bar{t}$ is mixture of the two, with a branching ratio very similar to the fully hadronic decay mode, but has some of the advantages and disadvantages of the two former decay modes. With each decay mode having advantages and disadvantages, there is ample motivation to explore each of them in order to maximize the prospects of discovery.

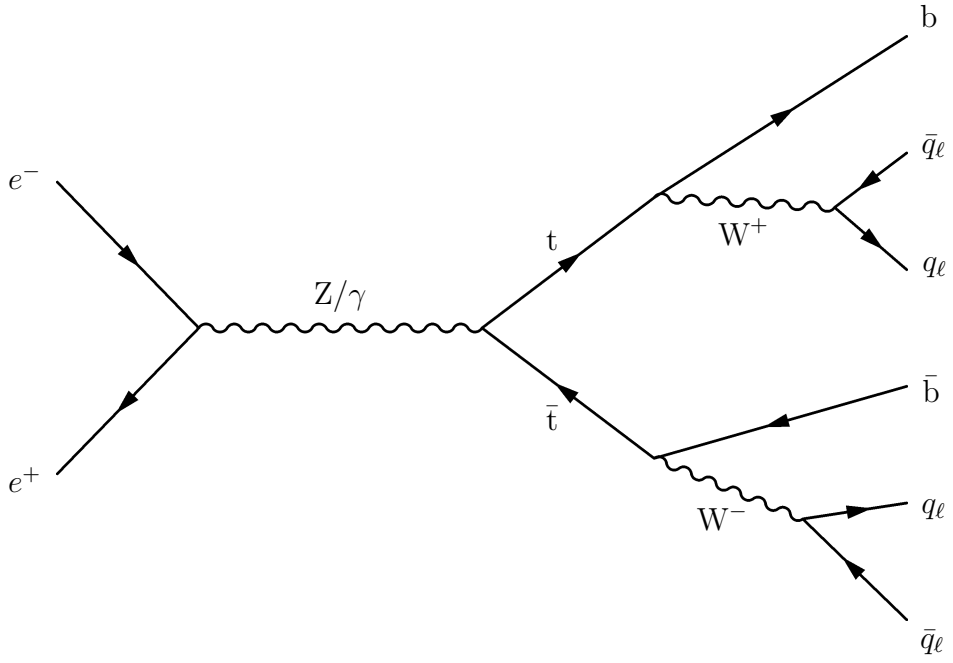

Figure 5.1: The Feynman diagram showing the full process including the subsequent hadronic decays of the top quarks.

5.2 Backgrounds

The vast majority of events will not have any top quarks. These events can however have final states that resemble the final state of the signal. These events are known as background, and the ability to distinguish and therefore seperate the background from the signal is of great importance. The considered backgrounds are meant to serve as a representative depiction of the amount and type of background that would occur in the real scenario in FCC. It is however not an exhaustive list, and processes exist that are not considered here. The integrated luminosity used in this project corresponds to the target luminosity of 1.5 ab^{-1} quoted in [4]. Given the timeline of the project it is reasonable to assume this target is not only feasible, but perhaps even a conservative number. All backgrounds considered in this thesis can be found along with their cross section and the expected number of events in 5.1. The number of expected events is easily calculated from the luminosity and the total cross section

$$N = \mathcal{L} \cdot \sigma \tag{5.2}$$

where L is the integrated luminosity and σ is the cross section.

Process	σ [pb]	Number of events
$t\bar{t} \to b\bar{b}q_\ell\bar{q}_\ell q_\ell\bar{q}_\ell$	$0.2065 \pm 1.292 \cdot 10^{-3}$	$309,750 \pm 1556$
$q_\ell\bar{q}_\ell$	$17.03 \pm 1.697 \cdot 10^{-3}$	$25,545,000 \pm 2531$
W^+W^-	$11.20 \pm 1.307 \cdot 10^{-3}$	$16,800,000 \pm 1961$
$b\bar{b}$	$4.065 \pm 7.920 \cdot 10^{-4}$	$6,097,500 \pm 1188$
$\mu^+\mu^-$	$1.902 \pm 4.720 \cdot 10^{-4}$	$2,853,000 \pm 708$
$\tau^+\tau^-$	$1.901 \pm 4.721 \cdot 10^{-4}$	$2,851,500 \pm 708$
ZZ	$0.8565 \pm 2.590 \cdot 10^{-4}$	$1,284,750 \pm 389$
ZH	$0.1296 \pm 1.230 \cdot 10^{-4}$	$194,400 \pm 185$
ZWW	$0.01594 \pm 1.735 \cdot 10^{-5}$	$23,910 \pm 26$
Single top	$4.572 \cdot 10^{-4} \pm 1.191 \cdot 10^{-5}$	6858 ± 18
ZZZ	$7.644 \cdot 10^{-4} \pm 2.632 \cdot 10^{-6}$	$1,147 \pm 4$

Table 5.1: Table of values of signal and all considered backgrounds along with their cross section and expected number of events at $1.5\,\text{ab}^{-1}$ and $\sqrt{s} = 365\,\text{GeV}$.

The first 7 backgrounds were simulated using Pythia. The last three backgrounds were simulated using **MadGraph** [14]. MadGraph produces an LHE file. The LHE files are imported with a Pythia command file in order to run the Delphes detector reconstruction as well as utilize the fragmentation in Pythia.

5.2.1 Effects of ISR and FSR

The processes simulated with Pythia all include initial state radiation (ISR) as well as final state radiation (FSR). These effects can be very significant depending on the specific process. In particular, processes with a peak at the $\sqrt{s} = m_Z$ are heavily

affected by ISR. This is due to the fact that the energy carried away by the ISR photons essentially shift the center of mass energy from $\sqrt{s} = 365\,\text{GeV}$ towards the Z-peak and thus increasing the total cross section. The opposite of this is seen with the $t\bar{t}$, where less energy available shifts the total cross section away from the peak, thereby lowering the cross section. MadGraph does not have ISR or FSR built in, and such the event samples for the last three backgrounds are not including ISR and FSR.

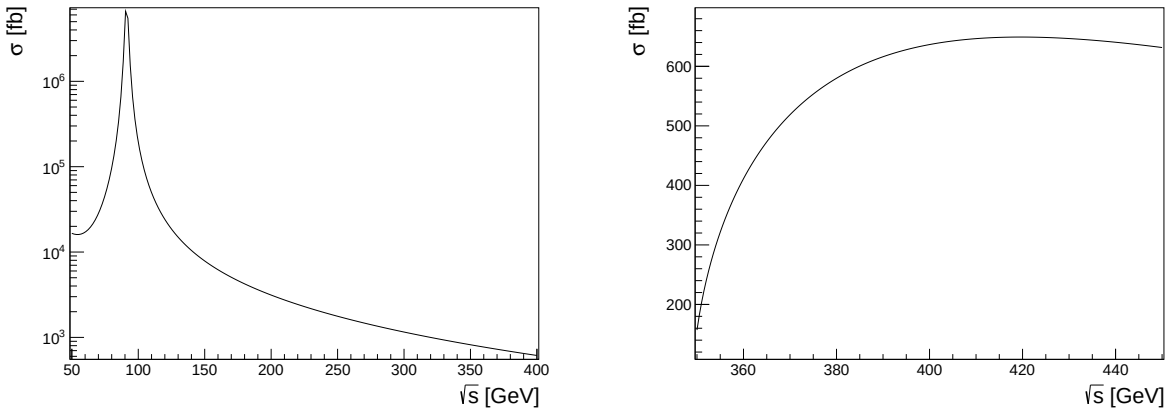

(a) $b\bar{b}$ (b) $t\bar{t}$

Figure 5.2: Total cross section as a function of $\sqrt{s}$.

5.3 Simulation of Anomalous Couplings

The simulation of all event samples with anomalous couplings enabled is done using **Whizard** [15]. Whizard is a program that enables efficient calculation and event sample simulation. The model file that includes the anomalous couplings are built-in inside the "SM_top_anom" file. The file includes the couplings described in section 3.1, however 3 of the couplings are kept fixed in order to preserve gauge invariance. In total, 14 event samples are produced corresponding to the 7 free parameters left over, each with an event sample for the coupling value $\alpha = 1$ and $\alpha = -1$, except for the coupling ΔV_R where $\alpha = \pm 0.5$. The couplings considered as well as their cross section can be seen in 5.2. The output of Whizard is in the form of LHE files similar to MadGraph. As with the event samples from MadGraph, the event samples from Whizard are imported with a Pythia command card in order to utilize the fragmentation capabilities of Pythia as well as the detector reconstruction of Delphes.

Coupling	α	σ [pb]
SM	0	0.2197
δV_L	+0.5	0.3775
	-0.5	0.2024
δV_R	+1	0.2196
	-1	0.2196
δg_L	+1	0.2196
	-1	0.2196
δg_R	+1	1.177
	-1	1.876
δd_V^γ	+1	1.306
	-1	3.370
δd_A^γ	+1	0.2956
	-1	0.2956
δX_{tt}^R	+1	0.3593
	-1	0.2206

Table 5.2: Cross sections for each of the anomalous couplings calculated by Whizard. All cross sections are normalized by the hadronic branching ratio. The SM cross section quoted is also from Whizard despite the event sample not being used.

Whizard does not have ISR and FSR built-in by default. This does introduce some complications that cannot be fully accounted for. The difference in cross section is accounted for by simply multiplying the cross sections by the ratio of the cross section found from Pythia that includes ISR, and that from Whizard that does not, with that factor being $0.2065\,\text{pb}/0.2197\,\text{pb} = 0.9399$. A more subtle complication arises from the fact that the energy scale Λ is also affected by ISR. This in turn means that the energy loss from ISR is effectively changing the strength of the anomalous couplings. This is however not possible to account for, unless ISR and FSR are implemented in Whizard, or, the anomalous couplings become available in Pythia.

6 Event Selection and Reconstruction

Event selection plays a vital role in particle physics, serving as a crucial step in the data analysis. The primary motivations behind this rigorous selection process is the necessity to reduce the amount of background events. When colliders create particle collisions, it is a given that not every event will be of interest. These background events, while important in their own right, can overshadow the signal events. This chapter describes the event selection process used in this project, as well as the reconstruction method of the kinematic fit employed in order to reconstruct the pair of top quarks.

6.1 Anatomy of a Fully Hadronic $t\bar{t}$ Event

In order to optimize the search for this particular process it is crucial for the search strategy to know exactly what these events look like in the detector. The fully hadronic $t\bar{t}$ events constitute a $2 \rightarrow 6$ event. With both of the W bosons decaying into two hadrons, the signature in the detector will have six hadronic jets, assuming they are all reconstructed properly, and not escaping detection by flying out along the beam pipe. In reality, there is an additional complication from final state gluon radiation. Because the final state quarks carry color charge, they can radiate off gluons that in turn will produce a gluon jet. In that case the final state will be a seven-jet structure. The application of the exclusive jet algorithm from FastJet in this project means the final state is "forced" to always have six jets, meaning that any potential gluon jets get combined with another jet. As a consequence, no particular effort has been put into studying the effects of additional gluon jets. Due to the hadronisation process inherent to the strong interaction described in section 2, the six hadronic jets are expected to produce a large amount of particles. Another key feature of the hadronic decay is a low amount of missing energy, since essentially all the final state products are expected to show up in the detector. Lastly, the b-quarks from the decay of the t-quarks makes efficient b-tagging of the jets of great importance. Understanding and targeting the search for fully hadronic $t\bar{t}$ events based on these criteria, as well as others, are therefore an instrumental part of keeping the desired events, and equally important, removing the undesired events. Many observables can be used in order to seperate the signal from the background. An example of one such observable is the aplanarity. The aplanarity is an event shape observable, meaning it contains information about how events appear in the detector. A momentum tensor can be defined as

$$M_{xyz} = \sum_i \begin{pmatrix} p_{xi}^2 & p_{xi}p_{yi} & p_{xi}p_{zi} \\ p_{yi}p_{xi} & p_{yi}^2 & p_{yi}p_{zi} \\ p_{zi}p_{xi} & p_{zi}p_{yi} & p_{zi}^2 \end{pmatrix} \tag{6.1}$$

where the sum is over all the reconstructed jets. Ordering and normalizing the three eigenvalues of the tensor such that $\lambda_1 > \lambda_2 > \lambda_3$ and $\sum_i \lambda_i = 1$, the sphericity, transverse sphericity as well as the aplanarity can be defined as

$$S = \frac{3}{2}(\lambda_2 + \lambda_3), \qquad S_\perp = \frac{2\lambda_2}{\lambda_1 + \lambda_2}, \qquad A = \frac{3}{2}\lambda_3 \tag{6.2}$$

The observable of interest is the aplanarity, A, and is a measure of the amount of momentum going in or out of the plane formed by the two leading jets. In a fully

hadronic $t\bar{t}$ event, many reconstructed particles are expected without a strong preference for any particular direction of those jets. It is therefore natural to expect that the hadronic $t\bar{t}$ events will have, on average, a distribution of aplanarity that is more spread out. In contrast, a $2 \to 2$ event e.g. $q\bar{q}$ with a very large amount of momentum being carried by each of the jets, most events are expected to have a relatively low measure of aplanarity.

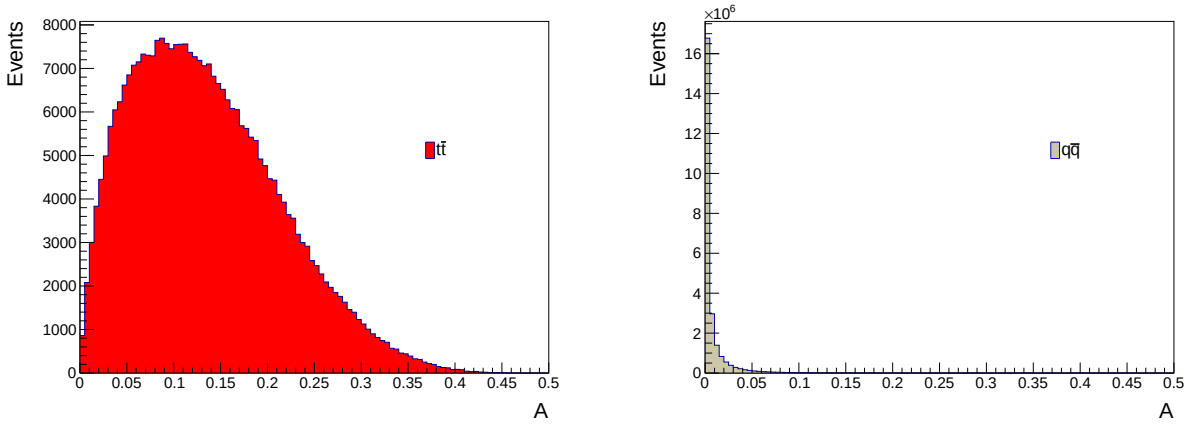

(a) signal (b) $q\bar{q}$

Figure 6.1: Distribution of aplanarity prior to cuts for $t\bar{t}$ and $q\bar{q}$.

6.2 Background Separation

In order to seperate the desired $t\bar{t}$ events from all the background, cuts are made on certain variables that will exclude events based on the values of those observables. The optimal region is found based on the optimization of the three following quantities

$$\text{Significance} = \frac{S}{\sqrt{S+B}} \tag{6.3}$$

$$\text{Efficiency} = \frac{S}{S_{\text{total}}} \tag{6.4}$$

$$\text{Purity} = \frac{S}{S+B} \tag{6.5}$$

where S is the number of selected signal events, S_{total} is the amount of total signal events and B is the number of selected background events. The significance determines how many standard deviations the signal exceeds statistical fluctuations. The efficiency is a measure of the fraction of signal events that are preserved and the purity is the fraction of signal events among the total number of events. Optimizing for significance is often a good strategy when the goal of the analysis is the discovery of new physics. A high-significance result hints at a strong signal, one that is unlikely to be a mere product of random statistical fluctuations, thus enhancing the statistical robustness of the analysis. However optimizing for purity can be beneficial if background events are important to filter out. A high purity ensures a greater fraction of signal events, making the signal easier to interpret among the noise. Moreover, a highly pure selection can reduce systematic uncertainties related to background estimation.The

major drawback lies in the potential loss of signal events. In the pursuit of minimizing background noise, many signal events might be discarded, thereby decreasing the efficiency. The optimization of efficiency aims to capture the maximum number of signal events. This approach is often optimal when dealing with rare or weak signals. However, by optimizing for high efficiency, it often comes with an increased amount of background events. This increase can reduce the purity of the data, making the signal more difficult to distinguish. Additionally, the inclusion of more background events can lead to increased systematic uncertainties, complicating the analysis. In many cases, the product of the purity and efficiency, PE is optimized. This is done in order to maximize the purity of the event sample while simultaneously minimize the loss of signal events. In this analysis, the event selection is optimized for the significance. It is worth noting the set of cuts that optimizes the significance is also the set of cuts that optimizes the product of purity and efficiency PE. The following variables are used for separating signal from background:

- Number of reconstructed particles
- Invariant mass
- Thrust
- Aplanarity
- Missing energy
- Missing momentum
- Minimum distance measure, d_{ij} $7 \to 6$
- Minimum distance measure, d_{ij} $6 \to 5$
- Number of b-tagged jets

where d_{ij} $7 \to 6$ is the minimum of the distance measure as defined in 4.5 of going from seven to six jets, and similarly, d_{ij} $6 \to 5$ of going from six to five jets. The event selection is carried out in two discrete steps. Firstly, a coarse initial event selection keeps only events where the FastJet algorithm can reconstruct seven jets. The jet algroithm is instructed to terminate at seven jets in order to calculate the d_{ij} $7 \to 6$ used in the event selection. The final iteration of going to six jets is then done after in order to end up ultimately with six jets. This initial selection already filters out the vast majority of $\mu\bar{\mu}$ and $\tau\bar{\tau}$ events as these mostly have very few particles in the final state. In the second step of the event selection process, the cuts corresponding to the maximum significance are performed. In general, a more narrow initial event selection that rejects background already at the first stage is to be preferred due to the computational efficiency of performing cuts on a smaller event sample.

6.2.1 TMVA

The background separation itself is done using the **Rectangular cut optimization** method available through the *Toolkit for Multivariate Analysis* (TMVA)[2], which is a

[2]Despite the name, the rectangular cut optimization method is not a multivariate method, but a sequence of univariate ones, since no combination of the variables is used.

library in ROOT. [16]. The rectangular cuts method, as the simplest method available in TMVA, offers a quick and easy-to-use option to separate signal and background. The method seeks to maximize the background rejection for a given signal efficiency by applying a series of upper and lower cuts on the discriminating variables used as input. The classifier then returns a simple binary response (signal or background) and simply counts the amount of signal events versus the amount of background events. The set of cuts that optimizes the significance as defined in 6.3 is then saved. Only events that pass the cuts are saved. If used on variables with strong separation of signal and background, the rectangular cut method is very competitive with more advanced classifiers. The simplicity of the method also means that it is more robust and less prone to overtraining, which can be an issue for more involved multivariate methods. A qualitative depiction of the rectangular cuts method can be seen in 6.2.

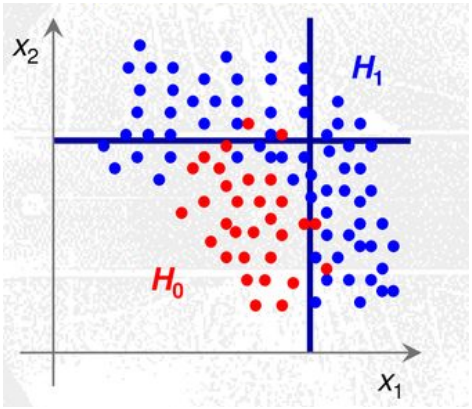

Figure 6.2: Rectangular cuts method example in two dimensions [17].

As an example, the distribution of the number of reconstructed particles is shown before and after applying cuts in 6.3. Prior to the application of cuts the signal is barely visible among all the background events.

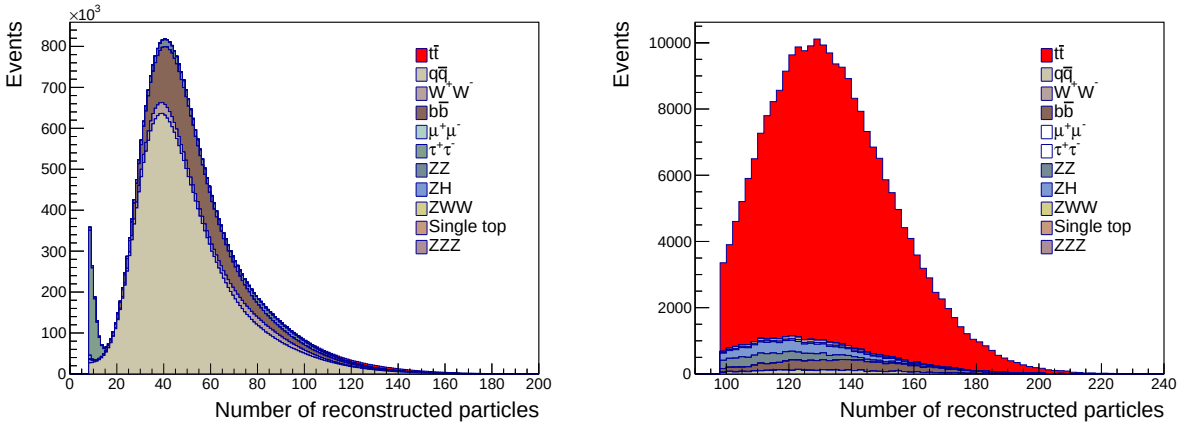

(a) Signal and background prior to cuts.

(b) Selected events after applying cuts.

Figure 6.3: Distribution of the number of reconstructed particles before and after applying cuts.

The set of cuts that maximizes the significance can be found in 6.1. In some of the

distributions, the signal is concentrated in either the bottom or top of the distribution. In that case, no cut is necessary.

Observable	Lower cut	Upper cut
Number of reconstructed particles	97	N/A
Invariant mass	301.5 GeV	N/A
Thrust	0.32	0.83
Aplanarity	0.04	0.45
Missing energy	N/A	94.5 GeV
Missing momentum	N/A	82.3 GeV
Minimum distance measure, d_{ij} $7 \to 6$	0.016	2.1
Minimum distance measure, d_{ij} $6 \to 5$	0.16	5.5
Number of b-tagged jets	1	N/A

Table 6.1: Lower and upper cut for each observable. N/A refers to no cut being made.

The number of events before and after applying cuts for both the signal and all background processes can be found in 6.2.

Process	N_{initial}	N_{selected}
$t\bar{t} \to b\bar{b}q_\ell\bar{q}_\ell q_\ell\bar{q}_\ell$	309,750	227,325
$q_\ell\bar{q}_\ell$	25,419,195	3,264
W^+W^-	15,212,521	1,904
$b\bar{b}$	6,090,743	9,034
$\mu^+\mu^-$	13,128	0
$\tau^+\tau^-$	866,604	0
ZZ	1,176,180	5,891
ZH	191,373	7,304
ZWW	23,390	1,152
Single top	6,858	1,993
ZZZ	1,131	140

Table 6.2: Number of events after initial selection and number of events after application of cuts for each process.

The application of cuts increases the significance of the signal region from 44.1 to 447.4. In the end, 73% of the signal is preserved, while simultaneously rejecting 99.94% of the background. Despite the very large number of $q_\ell\bar{q}_\ell$ events, their distributions of the observables used in the event selection process means that they are easily separated

from the signal. Conversely, single top events resemble $t\bar{t}$ very closely, and as such are much harder to filter out, despite the very low cross section.

	Significance	ϵ_S	ϵ_B
Initial	44.1	1.0	1.0
After selection	447.4	0.73	0.00062

Table 6.3: Significance, signal efficiency and background efficiency before and after applying cuts.

6.3 Kinematic Fit

The derivations in the following sections are based on [18] and [11]. The final state of the hadronic $t\bar{t}$ events appearing in the detector is six jets. The ultimate goal is to obtain knowledge about the $t\bar{t}$ pair itself at the quark level. This is however a very difficult task since in general, it is difficult to know which measured jet corresponds to which top quark. Additionally, the the limited detector resolution combined with particles escaping detection introduces effects that make reconstruction of the original quarks of the decay particularly difficult. In this analysis, the reconstruction at the quark level is performed with a kinematic fit. The fit is based on the method of least squares, which is a simple but effective method. At its core, the method of least squares seeks to minimize the sum of squares of deviations between a model and the data

$$S = \sum_{i=1}^{n} \Delta y_i^2 = \min \tag{6.6}$$

This method is used to determine corrections to the measurements of the jets in the effort to improve the accuracy of the reconstruction. The type of fitting is particular powerful when applied at lepton colliders, since the total energy as well as the momentum in directions are well known. This is not the case for hadron colliders where p_z is not known due to the composite nature of the proton and the complexities that follow.

6.4 Kinematic fit with constraints

The kinematic fit using the least squares method is used by imposing a set of constraints. The constraints are based on kinematic variables govern the specific $t\bar{t}$ process. The simplest constraints pertain to the conservation of energy and momentum in the event i.e.

$$\sum \begin{pmatrix} E \\ p_x \\ p_y \\ p_z \end{pmatrix} = \begin{pmatrix} 365 \\ 0 \\ 0 \\ 0 \end{pmatrix} \text{GeV} \tag{6.7}$$

Beyond these four constraints, additional four constraints are placed on the invariant masses of $t\bar{t}$-pair as well as the pair of W-bosons. In total, eight constraints are imposed in the kinematic fit. The model for a system of a total of m constraints can be expressed as

$$f_k(\mathbf{a}, \mathbf{y}) = 0, \qquad k = 1, \ldots, m \tag{6.8}$$

where $\mathbf{y}$ is a vector of n measurements, $\mathbf{a}$ is a vector of p unmeasured parameters. Assuming uncorrelated measurements, a covariance matrix $\mathbf{V}$ is given by the diagonal matrix

$$\mathbf{V} = \delta_{ij}\sigma_i\sigma_j \tag{6.9}$$

where σ_i is the resolution of measurement i. The principle of least squares is then to minimize

$$S(\mathbf{a}, \mathbf{y}) = \Delta\mathbf{y}^T\mathbf{V}(y)^{-1}\Delta\mathbf{y} \tag{6.10}$$

with respect to $\Delta\mathbf{y}$, where $\Delta\mathbf{y}$ is the vector of corrections to the measurements $\mathbf{y}$ such that

$$f_k(\mathbf{a}, \mathbf{y} + \Delta\mathbf{y}) = 0, \qquad k = 1, 2, \ldots m \tag{6.11}$$

Additional m parameters λ_k are introduced in the form of Lagrangian multipliers

$$L(\mathbf{a}, \Delta\mathbf{y}) = S(\mathbf{a}, \Delta\mathbf{y}) + 2\sum_{k=1}^{m} \lambda_k f_k(\mathbf{a}, \mathbf{y} + \Delta\mathbf{y}) \tag{6.12}$$

With the introduction of Lagrange multipliers, the necessary condition for a local extremum of this function with respect to $\Delta\mathbf{y}$. $\mathbf{a}$ and λ corresponds to the condition of a minimum of $S(\mathbf{a}, \Delta\mathbf{y})$ under the the conditions

$$f_k(\mathbf{a}, \mathbf{y} + \Delta\mathbf{y}) = 0 \tag{6.13}$$

Meaning that minimizing $S(\mathbf{a}, \Delta\mathbf{y})$ simultaneously fulfills

$$\frac{\partial L}{\partial y} = 0, \qquad \frac{\partial L}{\partial a} = 0, \qquad \frac{\partial L}{\partial \lambda} = 0 \tag{6.14}$$

For complicated system this is generally done in an iterative manner, since in general only linear problems can be solve analytically. In the case of non-linear conditions, the solution is found numerically by linearization of the conditions by a Taylor expansion

$$f_k(a^n, y^n) + \sum_j \frac{\partial f_k}{\partial a_j^{n+1}}(\Delta a_j^{n+1} - \Delta a_j^n) + \sum_i \frac{\partial f_k}{\partial y_i^{n+1}}(\Delta y_i^{n+1} - \Delta y_i^n) \approx 0 \tag{6.15}$$

The function L with linearization of constraints is given by

$$L = \Delta\mathbf{y}\mathbf{V}(\mathbf{y})^{-1}\Delta\mathbf{y} + 2\Lambda^T(\mathbf{A}\Delta\mathbf{a} + \mathbf{B}\Delta\mathbf{y} - \mathbf{c}) \tag{6.16}$$

where $\mathbf{c}$ is given by

$$\mathbf{c} = \mathbf{A}\Delta\mathbf{a} + \mathbf{B}\Delta\mathbf{y} - \mathbf{f} \tag{6.17}$$

and $\mathbf{A}$, $\mathbf{B}$ and $\mathbf{f}$ are given by

$$\mathbf{A} = \begin{pmatrix} \partial f_1/\partial a_1 & \partial f_1 \partial a_2 & \ldots & \partial f_1/\partial a_p \\ \partial f_2/\partial a_1 & \partial f_2 \partial a_2 & \ldots & \partial f_2/\partial a_p \\ \ldots & \ldots & \ddots & \ldots \\ \partial f_m/\partial a_1 & \partial f_m/\partial a_2 & \ldots & \partial f_m/\partial a_p \end{pmatrix}, \qquad \mathbf{f} = \begin{pmatrix} f_1(a^n, y^n) \\ f_2(a^n, y^n) \\ \ldots \\ f_m(a^n, y^n) \end{pmatrix} \tag{6.18}$$

(6.19)

$$\mathbf{B} = \begin{pmatrix} \partial f_1/\partial y_1 & \partial f_1 \partial y_2 & \ldots & \partial f_1/\partial y_n \\ \partial f_2/\partial y_1 & \partial f_2 \partial y_2 & \ldots & \partial f_2/\partial y_n \\ \ldots & \ldots & \ddots & \ldots \\ \partial f_m/\partial y_1 & \partial f_m/\partial y_2 & \ldots & \partial f_m/\partial y_n \end{pmatrix} \tag{6.20}$$

The system system of equations to be solved can be written of the form

$$\begin{pmatrix} \mathbf{V}^{-1} & 0 & \mathbf{B}^T \\ 0 & 0 & \mathbf{A}^T \\ \mathbf{B} & \mathbf{A} & 0 \end{pmatrix} \begin{pmatrix} \Delta\mathbf{y} \\ \Delta\mathbf{a} \\ \lambda \end{pmatrix} = \begin{pmatrix} 0 \\ 0 \\ \mathbf{c} \end{pmatrix} \tag{6.21}$$

The solution is given by the inverse

$$\begin{pmatrix} \Delta\mathbf{y} \\ \Delta\mathbf{a} \\ \lambda \end{pmatrix} = \begin{pmatrix} \mathbf{V}^{-1} & 0 & \mathbf{B}^T \\ 0 & 0 & \mathbf{A}^T \\ \mathbf{B} & \mathbf{A} & 0 \end{pmatrix}^{-1} \begin{pmatrix} 0 \\ 0 \\ \mathbf{c} \end{pmatrix} = \begin{pmatrix} \mathbf{C}_{11} & \mathbf{C}_{21}^T & \mathbf{C}_{31}^T \\ \mathbf{C}_{21} & \mathbf{C}_{22} & \mathbf{C}_{32}^T \\ \mathbf{C}_{31} & \mathbf{C}_{32} & \mathbf{C}_{33} \end{pmatrix} \begin{pmatrix} 0 \\ 0 \\ \mathbf{c} \end{pmatrix} = \begin{pmatrix} \mathbf{C}_{31}^T \\ \mathbf{C}_{32}^T \\ \mathbf{C}_{33} \end{pmatrix} \mathbf{c} \tag{6.22}$$

Where the individual elements are given by

$$\begin{aligned} \mathbf{C}_{11} &= \mathbf{V} - \mathbf{V}\mathbf{B}^T\mathbf{W}_B\mathbf{B}\mathbf{V} + \mathbf{V}\mathbf{B}^T\mathbf{W}_B\mathbf{A}\mathbf{W}_A^{-1}\mathbf{A}^T\mathbf{W}_B\mathbf{B}\mathbf{V} \\ \mathbf{C}_{21} &= -\mathbf{W}_A^{-1}\mathbf{A}^T\mathbf{W}_B\mathbf{B}\mathbf{V} \\ \mathbf{C}_{22} &= \mathbf{W}_A^{-1} \\ \mathbf{C}_{31} &= \mathbf{W}_B\mathbf{B}\mathbf{V} - \mathbf{W}_B\mathbf{A}\mathbf{W}_A^{-1}\mathbf{A}^T\mathbf{W}_B\mathbf{B}\mathbf{V} \\ \mathbf{C}_{32} &= \mathbf{W}_B\mathbf{A}\mathbf{W}_A^{-1} \\ \mathbf{C}_{33} &= -\mathbf{W}_B + \mathbf{W}_B\mathbf{A}\mathbf{W}_A^{-1}\mathbf{A}^T\mathbf{W}_B \end{aligned} \tag{6.23}$$

where $\mathbf{W}_B = (\mathbf{B}\mathbf{V}\mathbf{B}^T)^{-1}$ and $\mathbf{W}_A^{-1} = (\mathbf{A}^T\mathbf{W}_B\mathbf{A})^{-1}$. The covariance matrix $\mathbf{V}$ symmetric, which means the elements $\mathbf{C}_{11}$, $\mathbf{C}_{22}$, $\mathbf{C}_{31}$ and $\mathbf{C}_{33}$ are also symmetric. The covariance matrix for the solution is given by

$$\mathbf{V}\begin{pmatrix} \hat{\mathbf{y}} \\ \hat{\mathbf{a}} \\ \hat{\lambda} \end{pmatrix} = \begin{pmatrix} \mathbf{C}_{11} & \mathbf{C}_{21}^T & 0 \\ \mathbf{C}_{21} & \mathbf{C}_{22} & 0 \\ 0 & 0 & -\mathbf{C}_{33} \end{pmatrix} \tag{6.24}$$

The final element in the fit is the inclusion of probability distribution functions (PDF). Due to the Breit-Wigner nature of unstable particles, the masses of the reconstructed top quarks and W-bosons are not expected to be exactly on resonance. This behavior is accounted for by introducing a probability distribution function which extends the function L such that

$$L(\mathbf{a}, \Delta\mathbf{y}) = S(\mathbf{a}, \Delta\mathbf{y}) + g(x) + 2\sum_{k=1}^{m} \lambda_k f_k(\mathbf{a}, \mathbf{y} + \Delta\mathbf{y}) \tag{6.25}$$

where the function $g(x)$ has been included. $g(x)$ represents a penalty function, meaning the constraint is loosened but comes with a penalty of violating that constraint. The inclusion of the PDF can be included by extending the $\mathbf{B}$-matrix in order to included total set of measured parameters $\{\mathbf{y}, x\}$

$$\mathbf{B} = \frac{\partial f(\mathbf{a}, \mathbf{y}, x)}{\partial(\mathbf{y}, x)} \tag{6.26}$$

as well as extending the covariance matrix such that

$$\tilde{\mathbf{V}} = \begin{pmatrix} \mathbf{V} & 0 \\ 0 & \left(\frac{1}{2}\frac{d^2g}{dx^2}|_{x=x^n}\right)^{-1} \end{pmatrix} \tag{6.27}$$

The corrected measured parameters in the $n+1$-th iteration are now given by

$$\begin{pmatrix} y^{n+1} \\ x^{n+1} \end{pmatrix} = \begin{pmatrix} y_0 \\ x^n \end{pmatrix} - \tilde{\mathbf{V}} \begin{pmatrix} 0 \\ \frac{1}{2}\frac{d^2g}{dx^2}|_{x=x^n} \end{pmatrix} + \tilde{\mathbf{V}}\mathbf{B}^T(\mathbf{B}\tilde{\mathbf{V}}\mathbf{B}^T)^{-1} \times \left[A(a^n - a_0) + B \begin{pmatrix} y^n - y_0 \\ \frac{dg}{dx}|^{-1}_{x=x^n} / \frac{d^2g}{dx^2}|_{x=x^n} \end{pmatrix} - f(a^n, y^n, x^n) \right]$$

and the corrected free parameters in the $n+1$-th iteration are now given by

$$a^{n+1} = a_0 + \mathbf{W}_A^{-1} A^T \mathbf{W}_B \times \left[A(a^n - a_0) + B \begin{pmatrix} y^n - y_0 \\ \frac{dg}{dx}|^{-1}_{x=x^n} / \frac{d^2g}{dx^2}|_{x=x^n} \end{pmatrix} - f(a^n, y^n, x^n) \right]$$

6.5 ABC-parameterization

The constrained fit is parameterized in terms of the 3-vector of the reconstructed particle

$$\vec{p_j}^{\,r} = a_j |\vec{p_j}^{\,m}| \vec{p_j}^{\,a} + b_j \vec{p_j}^{\,b} + c_j \vec{p_j}^{\,c} \tag{6.28}$$

where a_j, b_j and c_j are parameters to be used in the fit, and $\vec{p_j}^{\,a}$ $\vec{p_j}^{\,b}$ and $\vec{p_j}^{\,c}$ are unit vectors that from a Cartesian coordinates system. They are found from the momentum of the measured jet $\vec{p_j}^{\,m}$ and are given by

$$\vec{p_j}^{\,a} = \frac{\vec{p_j}^{\,m}}{|\vec{p_j}^{\,m}|} \tag{6.29}$$

$$\vec{p_j}^{\,b} = \frac{1}{\sqrt{p_{x,m}^2 + p_{y,m}^2}} (p_y^m, -p_x^m, 0) \tag{6.30}$$

$$\vec{p_j}^{\,c} = \frac{1}{\sqrt{|\vec{p_j}^{\,m}|^2 (p_{x,m}^2 + p_{x,m}^2)}} (-p_x^m p_z^m, -p_y^m p_z^m, p_{x,m}^2 + p_{y,m}^2) \tag{6.31}$$

where $\vec{p_j}^{\,a}$ is defined such that it is in the direction of of measured jet, $\vec{p_j}^{\,b}$ is defined such that $\vec{p_j}^{\,a} \cdot \vec{p_j}^{\,b} = 0$ and $\vec{p_j}^{\,c}$ is defined as $\vec{p_j}^{\,a} \times \vec{p_j}^{\,b}$. Initially, the values of a_j, b_j and c_j are set to 1, 0 and 0 respectively, such that the reconstructed particle vector overlaps with the measured particle vector.

6.6 ABCfit++ software

The kinematic fit is implemented through the *ABC*-parameterization is implemented with the ABCfit++ software package [19]. The software package contains multiple classes that together make the fitting procedure possible. A detailed description of individual classes can be found in [11].

6.7 Fitting procedure

Prior to the fitting procedure, the a, b and c-parameters as well as the Gaussian parameters of the reconstructed top quarks and W-bosons that go into the fit are estimated. The spread of the a, b and c-parameters determine the resolutions that appear in the covariance matrix as defined in 6.9 to be used in the fit. In the fit, a

constraint is placed on the invariant mass of the top quark as well as the W-boson. At the quark level the spread in the distribution of the mass is from the associated Breit-Wigner distribution of unstable particles. However, this is not the full picture since at the detector level there is some amount of Gaussian spread of the energy. The resulting true spread is therefore a complicated convolution of a Gaussian with the Breit-Wigner distribution. In order to estimate an appropriate value of this spread to be used in the fit, several aspects can be considered. Below, a simple Gaussian is fitted to the distribution of the top and W mass. The distributions of both the a, b and c-parameters as well as the distribution of the invariant masses are found by matching the measured jets to the true value of the Monte Carlo particles. The unique matching is done by pairing the quark to the reconstructed jet closest in angle. The matching is such that only events where there is a unique match of the true Monte Carlo particles to the corresponding reconstructed jets are considered. The distribution of the a, b and c parameters for b-jets and hadronic jets from the W-bosons are shown in 6.4 and 6.5.

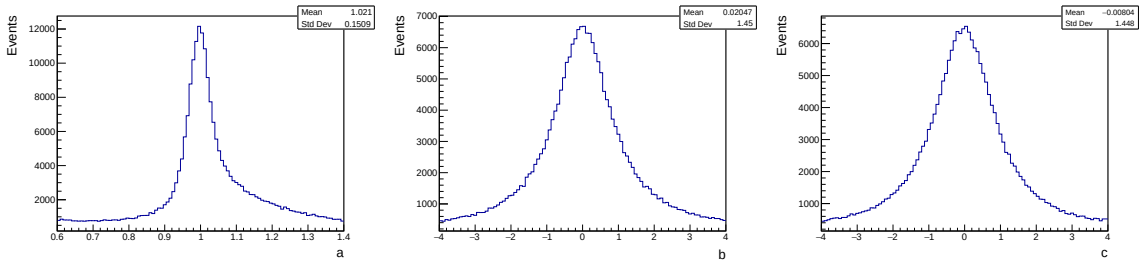

Figure 6.4: a,b and c parameters for b-jets.

Similarly for reconstructed jets from the hadronic W-decays

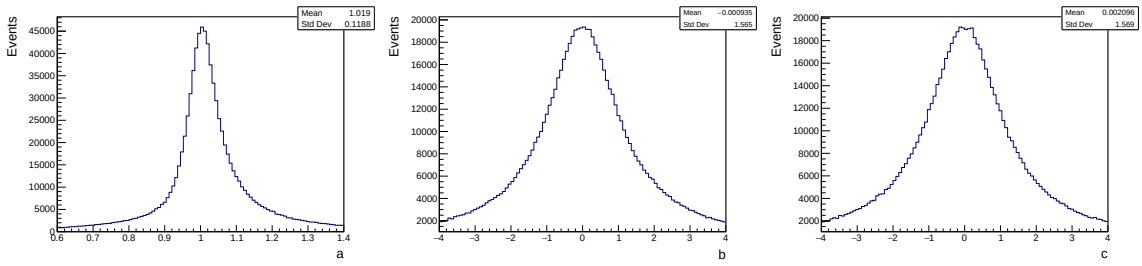

Figure 6.5: a,b and c parameters for W-decay jets.

In the central region the parameters are, to a good approximation, distributed according to a Gaussian. The values for the resolution of the b-jets are found to be

$$a = 0.15, \qquad b = 1.45, \qquad c = 1.45 \tag{6.32}$$

and similarly for the hadronic jets from the W-bosons

$$a = 0.12, \qquad b = 1.57, \qquad c = 1.57 \tag{6.33}$$

These values are used in the covariance matrices of the b-jets and the jets originating from the W-bosons to be used on the full data set of reconstructed particles. The

covariance matrices are determined to be

$$V_b = \begin{pmatrix} 0.15 & 0 & 0 & 0 \\ 0 & 1.45 & 0 & 0 \\ 0 & 0 & 1.45 & 0 \\ 0 & 0 & 0 & d_B \end{pmatrix} \qquad V_W = \begin{pmatrix} 0.12 & 0 & 0 & 0 \\ 0 & 1.57 & 0 & 0 \\ 0 & 0 & 1.57 & 0 \\ 0 & 0 & 0 & d_W \end{pmatrix} \tag{6.34}$$

The d-parameters refers to the mass resolution. This parameter is not used in the fitting procedure, as the masses of jets are simply kept fixed. The covariance matrices for both the b-jets as well as the hadronic jets from the W-bosons are assumed to be diagonal, i.e. all matrix elements outside of the diagonal are 0. This assumes that all measured jets are completely uncorrelated which is almost certainly not the case.

The following plots show the distribution of invariant mass of reconstructed top quarks and W-bosons found by the unique angular matching as described above. In this first set of plots, no constraints are placed. In the second set of plots, simple energy and momentum constraints are placed, i.e. the total event must fulfill

$$\sum \begin{pmatrix} E \\ p_x \\ p_y \\ p_z \end{pmatrix} = \begin{pmatrix} 365 \\ 0 \\ 0 \\ 0 \end{pmatrix} \text{GeV} \tag{6.35}$$

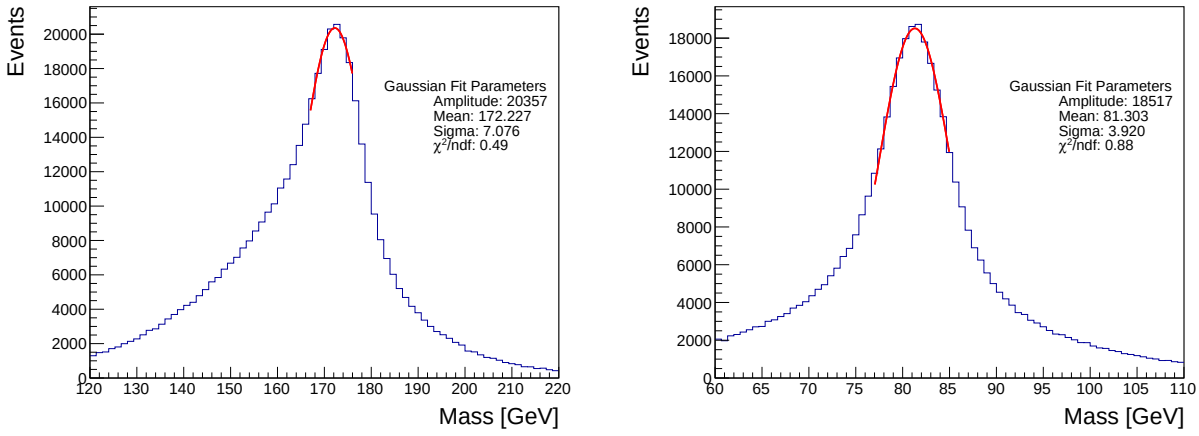

(a) Reconstructed top quarks.

(b) Reconstructed W bosons.

Figure 6.6: Distribution of invariant mass of the reconstructed top quarks (left) and the reconstructed W bosons (right) with Gaussian fit to the peak.

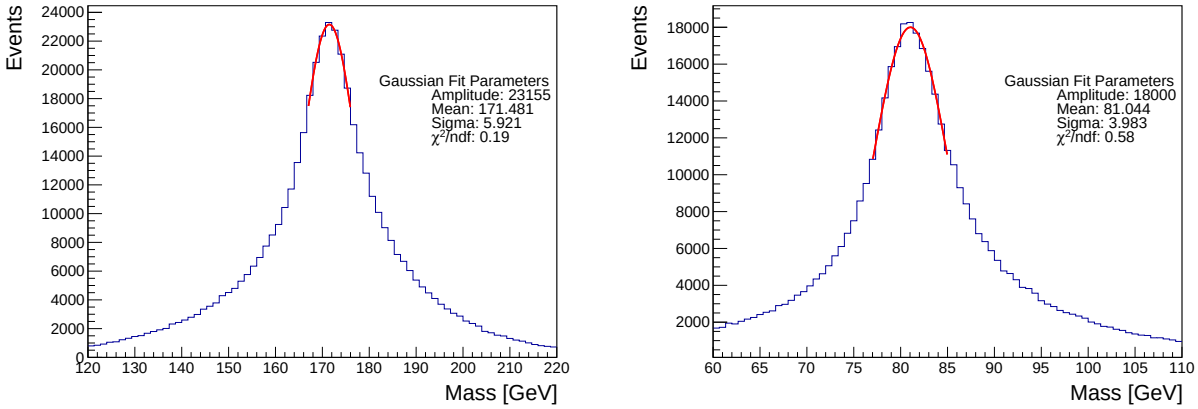

(a) Reconstructed top quarks.

(b) Reconstructed W bosons.

Figure 6.7: Distribution of invariant mass of the reconstructed top quarks (left) and the reconstructed W bosons (right) with four-vector constraints, with a Gaussian fit to the peak.

From the Gaussian fit it can be seen that imposing energy and momentum constraints decreases the standard deviation and thereby improves the resolution of the reconstructed top masses. Simply using the values obtained from the Gaussian fits would overestimate the spread. Secondly, since the W-bosons are the decay products of the top quarks, it means they inherit part of their spread, and as such their resolutions are correlated. In order to reflect the width of the mass distribution at the quark level, the choice was made to use the decay width of the top quark and the W-boson as the Gaussian width parameter in the fit. The values used are $\Gamma_t = 1.42\,\text{GeV}$ and $\Gamma_W = 2.1\,\text{GeV}$ [13].

The objective of the kinematic fit is to correctly determine which measured jets correspond to the two top quarks as well as the two b-quarks and the two W-bosons, when recombined. In the case of the fully hadronic decay this is an immensely computationally demanding task. The combinatorics of the final state are as follows: Of the six jets, two jets combine to make the first W, another two jets combine to make up the second W, and the remaining two jets are b-jets. Combinatorically, this is equivalent to choosing four objects from a pile of six objects, and then arranging them into two piles with each pile having two items, and then assigning the remaining two objects and arranging them into a pile each. The number of ways to choose four objects from six is

$$C(6,4) = \frac{6!}{(4! \cdot (6-4)!)} = 15 \tag{6.36}$$

In total there are 15 ways to choose which objects go into the piles of size two. The number of ways to arrange the four chosen objects is given by

$$C(4,2) = \frac{4!}{2! \cdot (4-2)!} = 6 \tag{6.37}$$

In total there $15 \cdot 6 = 90$ ways to arrange six objects into four piles of two, and two piles of one. This means the kinematic fit has to iterate through 90 combinations in each event. At each iteration, the χ^2 is calculated, and the combinations with the lowest

χ^2 is kept. The kinematic fit returns the combination of jets that make up the two W-bosons, the two b-quarks, and which combination of these that make up the top pairs along with the corrections to their momenta found by the fit. Ideally, the b-tagged jets should be used which would dramatically reduce the number of combinations for the fit to iterate through. This in turn would optimize the computational aspect, allowing for the analysis of many more events in a fraction of the time. This turned out to be unpractical in this analysis, due in part to the efficiency of the b-tagging combined with the false positive rate. Not only does a large fraction of the events only have one b-tagged jet, a fraction of the events have three b-tagged jets. As a consequence, it was necessary to iterate through all 90 combinations regardless. More sophisticated techniques could be envisioned, where the b-tags could be used as the starting point in order to speed up the computational process. For this project, no such strategies were explored, and all 90 combinations were systemically checked for all events regardless of any b-tags. The application of the kinematic fit improves the resolution of the momenta and energy as well as the masses of the reconstructed t-quarks and W-bosons as seen in the figures from 6.8 to 6.13.

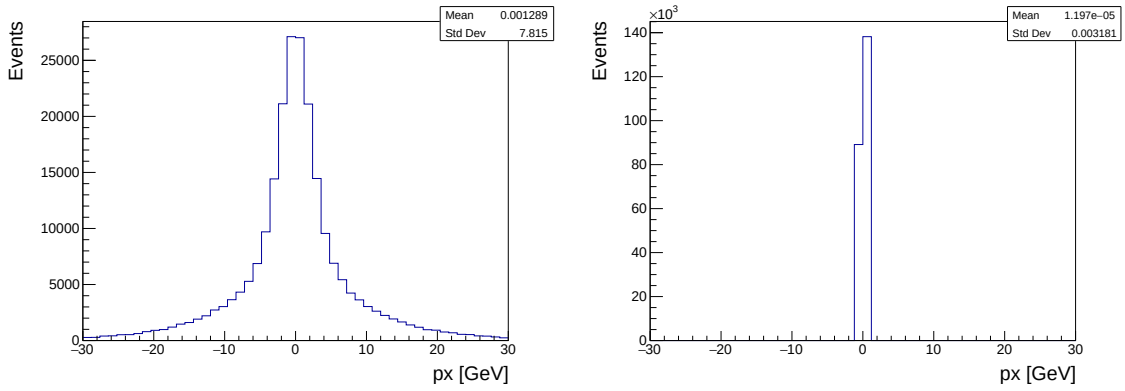

(a) Before fit. (b) After fit.

Figure 6.8: Total measured p_x before and after kinematic fit.

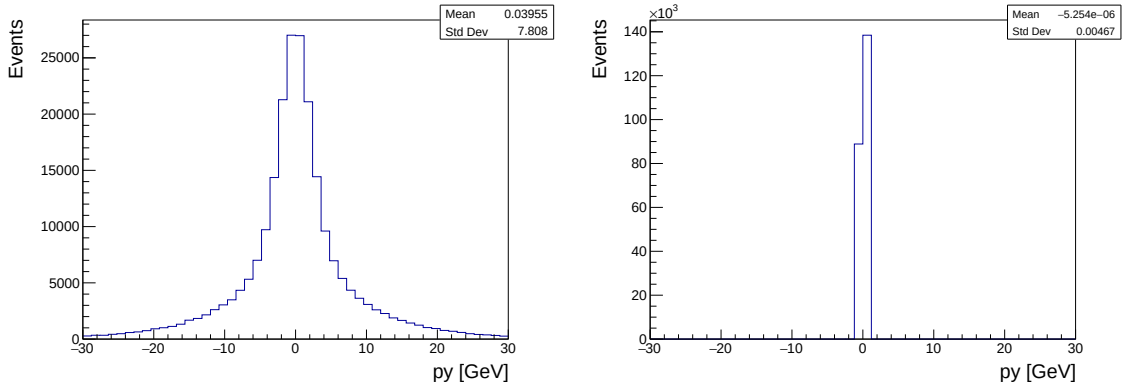

(a) Before fit. (b) After fit.

Figure 6.9: Total measured p_y before and after kinematic fit.

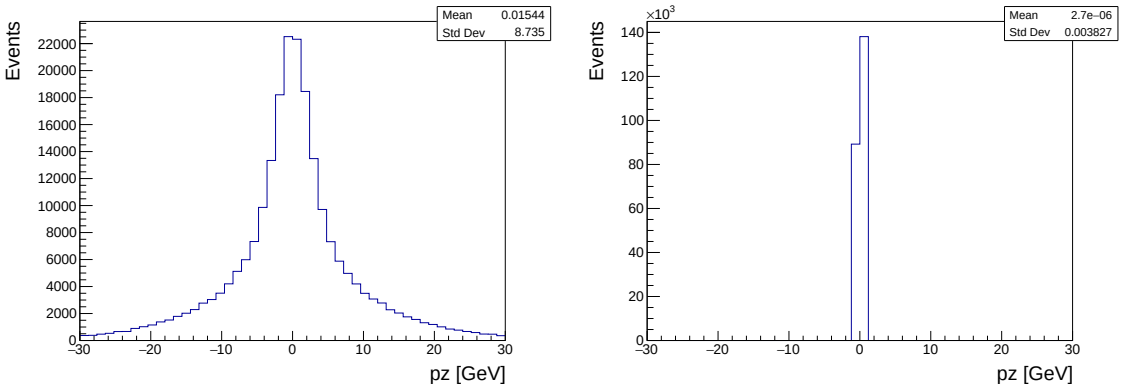

(a) Before fit. (b) After fit.

Figure 6.10: Total measured p_z before and after kinematic fit.

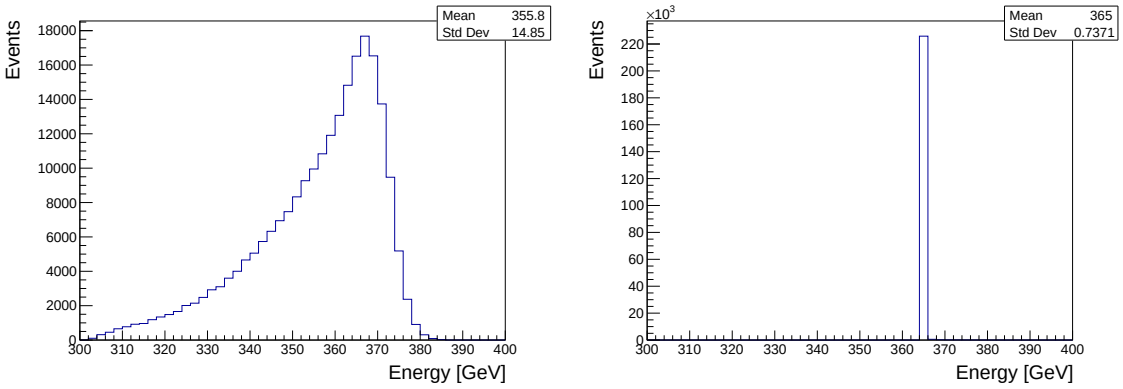

(a) Before fit. (b) After fit.

Figure 6.11: Total measured energy before and after kinematic fit.

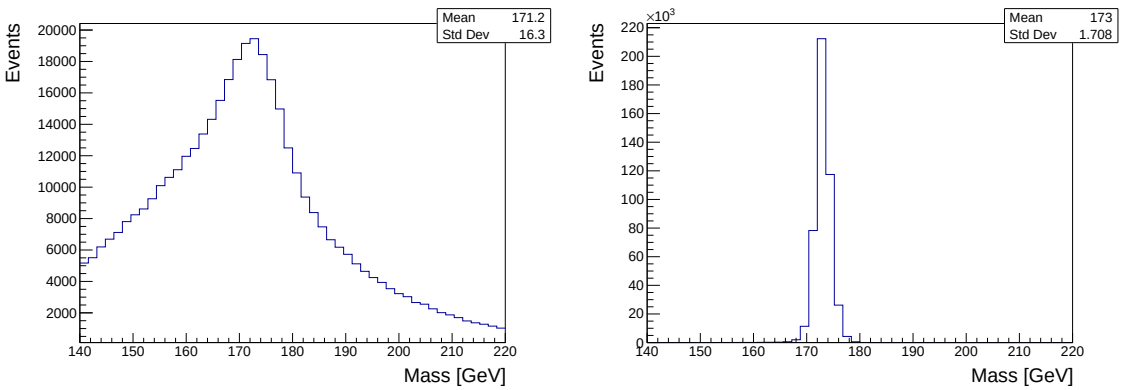

(a) Before fit. (b) After fit.

Figure 6.12: Invariant mass of reconstructed of t-quarks before and after kinematic fit.

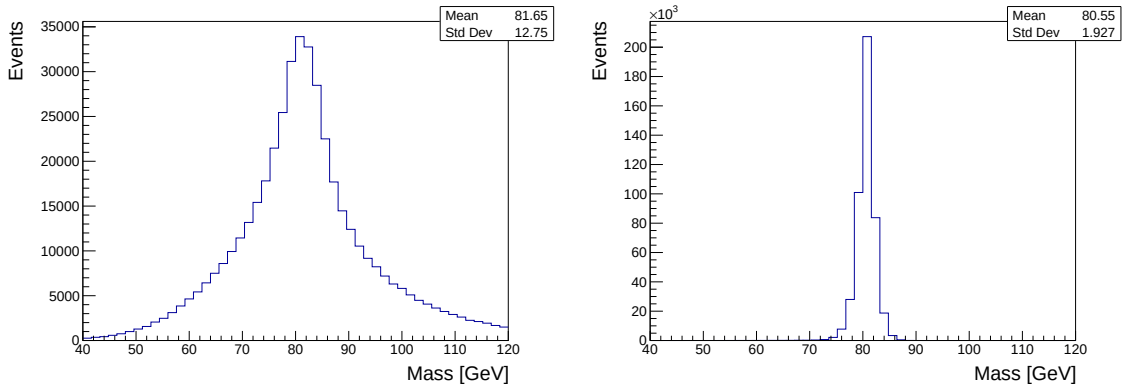

(a) Before fit.

(b) After fit.

Figure 6.13: Invariant mass of reconstructed of W-bosons before and after kinematic fit.

7 Analysis

This chapter presents the procedure used in this project of extracting the sensitivities to the individual anomalous couplings and the results obtained.

7.1 Observables

There are many approaches to investigate the effects of the anomalous couplings. In this thesis, the effects are studied by investigating angular distributions of the reconstructed top quarks and its decay products.

7.1.1 Angular distributions

The effects of the anomalous couplings are investigated by studying how they effect the angular distributions. The first angle of interest is the angle between the electron beam and the top quark

$$\cos(\theta_{et}) = \frac{\mathbf{p}_e \cdot \mathbf{p}_t}{|\mathbf{p}_e||\mathbf{p}_t|} \tag{7.1}$$

where $\mathbf{p}_e$ and $\mathbf{p}_t$ are the 3-momenta of the electron beam and the reconstructed top quark respectively, and $|\mathbf{p}_e|$ and $|\mathbf{p}_t|$ are the length of the respective vectors. The next angles of interest is the angle between the reconstructed top quark and its decay products in the reference frame of the top quark. This angle can be calculated by a Lorentz boost of the laboratory frame to the frame of the top quark. The angle is divided into the component parallel to the flight direction and the component perpendicular to the flight direction. The component parallel to the flight direction is given by

$$\mathbf{p}_{t_\parallel} = (\mathbf{p}_t \cdot \mathbf{p}_d)\frac{\mathbf{p}_t}{|\mathbf{p}|^2} \tag{7.2}$$

The perpendicular component of the angle is then simply

$$\mathbf{p}_{t_\perp} = \mathbf{p}_t - \mathbf{p}_{t_\parallel} \tag{7.3}$$

The perpendicular component of the angle is unaffected by the Lorentz boost. The parallel component of the angle, in the frame of the top, is given by

$$\mathbf{p}^*_{t_\parallel} = \gamma(\mathbf{p}_{t_\parallel} - \beta E) \tag{7.4}$$

where the star denotes the center of mass frame, and γ is the Lorentz factor. The polar angle between the top quark and its decay products can now be found from

$$\cos(\theta^*_{td}) = \frac{|\mathbf{p}^*_{t_\parallel}|}{\sqrt{(\mathbf{p}^*_{t_\parallel})^2 + (\mathbf{p}_{t_\perp})^2}} \tag{7.5}$$

Defining the flight direction of the top quark as the z-axis, the x-axis is defined as the cross product of the new z-axis and the axis defined by the beam direction x. To complete the right-handed coordinate system, the y-axis is given by the cross product of the newly defined z and x axes. The last angle of interest is the azimuthal angle, which is given by

$$\phi^* = \arctan\frac{\hat{\mathbf{y}} \cdot \mathbf{p}_d}{\hat{\mathbf{x}} \cdot \mathbf{p}_d} \tag{7.6}$$

The considered angles are summarized below.

$t\bar{t}$	$t \to bW$	
$\cos(\theta_{et})$	$\cos(\theta_{tb})$	ϕ^*_{tb}

Table 7.1: The three angles considered in the analysis.

The kinematic fit cannot distinguish the reconstructed t from the $\bar{t}$. Therefore the angular distributions will include both t and $\bar{t}$. In order to compensate the histograms are filled with a weight of 1/2 as to not overestimate the statistical weight of each event. The same is true for the b-quarks and the W-bosons. In the case of semi-leptonic as well as fully-leptonic $t\bar{t}$ events, the charge of the lepton(s) can be used in order to determine the charge of the t and in turn distinguish between t and $\bar{t}$. The absence of leptons makes the task for fully hadronic decays much more challenging. It could be envisioned to use the charge of potential leptons from the b decay as a possible way to determine the charge of the top. This was however not explored in this analysis.

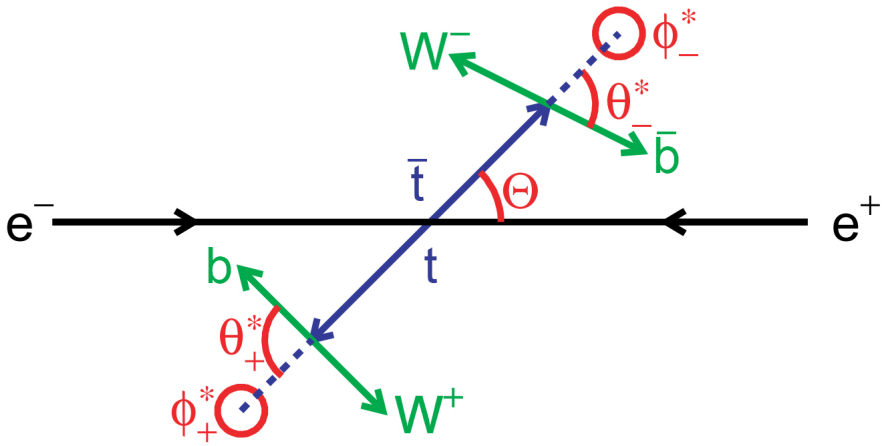

Figure 7.1: Illustration of the angles of interest. From [20].

7.2 Extraction of anomalous couplings

As described in section 3.2, the effective matrix element has a quadratic dependence on an individual anomalous couplings. As such the event samples with $\alpha = \pm 1$ together with the Standard Model event sample with $\alpha = 0$ make up three points that form a parabola. The angular distributions can then be parameterized in terms of the parameters A, B and C that describe the polynomial. The angular distributions in terms of these parameters can be written as

$$f(\alpha = 1) = A\alpha^2 + B\alpha + C \tag{7.7}$$
$$f(\alpha = -1) = A\alpha^2 - B\alpha + C \tag{7.8}$$
$$f(\alpha = 0) = C \tag{7.9}$$

The parameters A, B and C can be determined from this set of equations

$$A = \frac{f(\alpha = 1) + f(\alpha = -1)}{2\alpha^2} - \frac{f(\alpha = 0)}{\alpha^2} \tag{7.10}$$

$$B = \frac{f(\alpha = 1) - f(\alpha = -1)}{2\alpha} \tag{7.11}$$

$$C = f(\alpha = 0) \tag{7.12}$$

A fit is then performed to the angular distributions parameterized by A, B and C. A fit model can be introduced by

$$f(x) = Ax^2 + Bx + f(SM) + f(\text{Background}) \tag{7.13}$$

where the parameter C has been identified as f(SM) and background has been included as well. Confidence intervals can then be determined for each anomalous coupling by determining a χ^2 value

$$\chi^2 = \sum_{i=1}^{n} \frac{(y_i - f(x, \alpha))^2}{\sigma_{y_i}^2 + \sigma_{f(x_i,a)}^2} \tag{7.14}$$

where the term in the numerator is the difference between the observed value in the angular distribution and the value obtained in the fit model. The term in the denominator is the sum of the uncertainty from the square root of the bin and the fit model uncertainty from the number of simulated events. Ideally, the number of simulated events should far outweigh the number of expected events in order to reduce the error [3]. The sum is for each bin in the histogram. The Standard Model event sample is used to act as real data. By construction, the χ^2 is 0 for $\alpha = 0$, i.e. Standard Model event sample. The 1σ confidence intervals are the upper and lower value of α where $\chi^2 = 1$. As seen from 5.2, the couplings affect the cross section of the process. Both the cross section and the angular distributions contributes to to the sensitivity of the coupling. This information is included in the fit of the angular distributions by normalizing the individual distributions according to the respective cross section of the coupling. This is done for all angular distributions for each of the anomalous couplings separately.

7.3 Results

After applying the fit model described in eq 7.13 for the seven couplings, sensitivities are determined for all couplings for each angle. Based on the χ^2 fit, the best sensitivity is found from the $\cos(\theta_{et})$ distribution of the δd_V^γ coupling.

[3] Due to computational and time constraints, this is not the case for this analysis. The number of simulated events is similar to the number of events used and only surpasses by a small fraction.

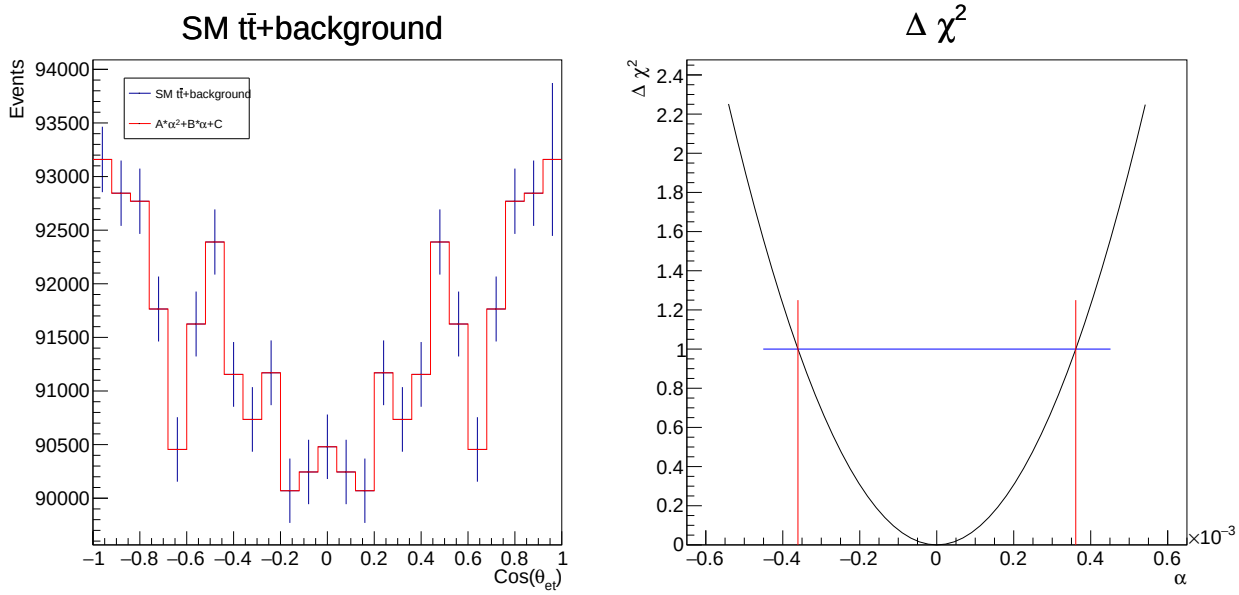

(a) Angular distribution with fit (b) χ^2 distribution and confidence interval

Figure 7.2: Angular distribution of $\cos(\theta_{et})$ and χ^2 distribution of coupling δd_V^γ.

The coupling with the least sensitivity is found from the fit to be the distribution of $\cos(\theta_{et})$ of the coupling δV_R

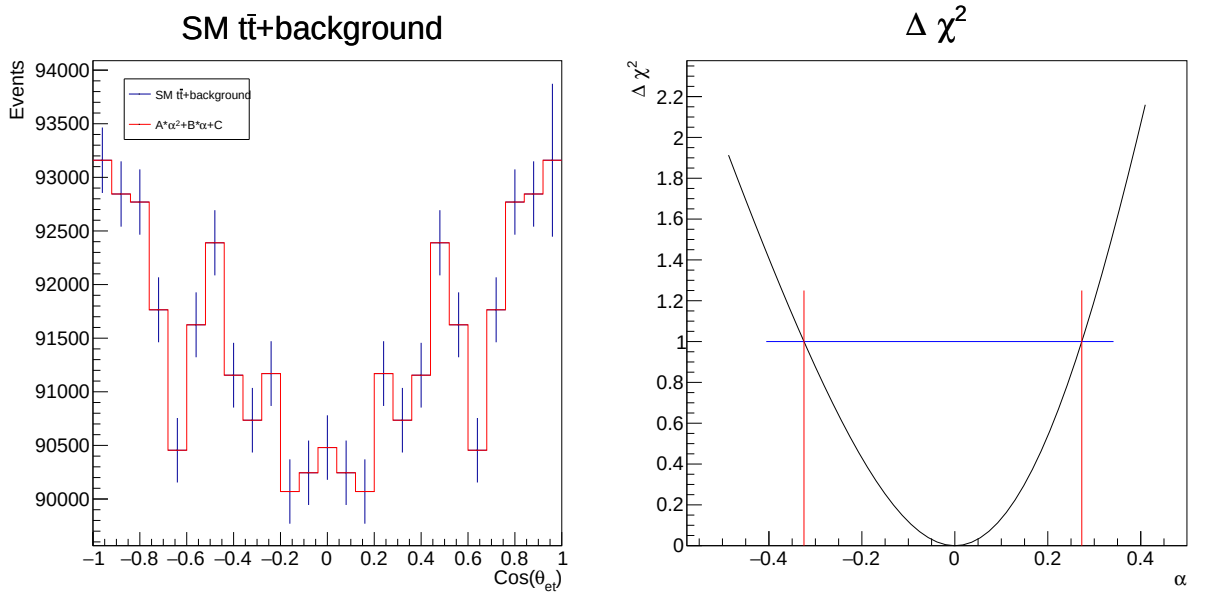

(a) Angular distribution with fit (b) χ^2 distribution and confidence interval

Figure 7.3: Angular distribution of $\cos(\theta_{et})$ and χ^2 distribution of coupling δV_R.

The table displaying all confidence intervals found for each coupling can be found in 7.2

Coupling	$\cos(\theta_{et})$	$\cos(\theta_{tb})$	ϕ_{tb}
δV_L	-0.0743761 0.0743761	-0.0741014 0.0741014	-0.0743729 0.0743729
δV_R	-0.324585 0.27315	-0.25623 0.2862	-0.264947 0.351174
δg_L	-0.187236 0.181414	-0.169006 0.174438	-0.182452 0.190001
δg_R	-0.00124483 0.00125749	-0.0012413 0.00125387	-0.00124739 0.00126008
δd_V^γ	-0.000360617 0.000361157	-0.000360208 0.000360743	-0.000361308 0.000361853
δd_A^γ	-0.0650069 0.0692615	-0.0668985 0.0717254	-0.0678436 0.0714862
δX_{tt}^R	-0.00539516 0.00533708	-0.00541099 0.00535208	-0.00540035 0.00534204

Table 7.2: Confidence intervals for all couplings for the three angles studied.

The couplings with the highest sensitivity are also the couplings where the total cross section are affected the most. Since both information about the angular distributions as well as the information about the total cross section is included in the fit, it is expected that this is the case. Similarly, the coupling with the lowest sensitivity, δV_R, there is no effect on the total cross section.

7.4 Discussion

As is always the case with projects that study the details of a subject matter, a set of choices must be made in regards to the analysis. These choices will inevitable affect and bias the results that are obtained. Whenever possible, an effort was applied in order to justify these choices. However, even justified choices are not guaranteed to be optimal. The use of angular distributions is a relatively simple set of observables that can be used to study the effects of anomalous couplings and determine the sensitivities. It is however not guaranteed to be the set of observables most sensitive to BSM effects. A more optimal strategy to search for BSM effects can be employed by constructing so called *optimal observables* [21], which by construction are particularly sensitive to BSM effects. The method of optimal observables works by projecting the kinematic information which is most sensitive to a particular parameter onto a single variable. Optimal observables can be defined in terms of the differential cross section

$$\frac{d\sigma}{d\Omega} = S_0(\Omega) + \sum_i S_{1,i}(\Omega)P_i + \sum_{ij} S_{2,ij}(\Omega)P_iP_j \tag{7.15}$$

where Ω is the full set of reconstructed kinematic variables e.g. different scattering angles. The idea is then to measure the distribution of the function

$$\mathcal{O}_i = \frac{S_{1,i}(\Omega)}{S_0(\Omega)} \tag{7.16}$$

where $\mathcal{O}_i$ is the optimal observable for coupling i. The method of optimal observables requires the full expression of the effective matrix element as defined in 3.11. The analytical calculation of matrix elements is made possible with the software package **FeynCalc** [22]. FeynCalc is a **Mathematica** [23] package designed for quantum field theory calculations, particularly useful for Dirac algebra, tensor reduction, and Feynman diagram calculations. The FeynCalc package also includes **FeynArts**, which is primarily used for the generation and visualization of Feynman diagrams and amplitudes. Lastly, **FeynRules** [24] is a Mathematica package used to calculate the Feynman rules for a given Lagrangian, which can then be exported to other codes. The Lagrangian of the model is specified within FeynRules. It is essential to include all the necessary fields, parameters, and their respective properties. Once the model is defined correctly, FeynRules can calculate the Feynman rules. These rules are then exported in a format that can be used with FeynArts. With the Feynman rules defined, FeynArts is utilized in order to generate the Feynman diagrams corresponding to the process. FeynArts offers the flexibility of generating diagrams based on a set of initial and final states defined by the user. Following the diagram generation, FeynArts calculates the corresponding amplitudes for each diagram, using the Feynman rules imported from FeynRules. The amplitudes obtained from FeynArts serve as input to FeynCalc. Here, the amplitudes are further simplified using various built-in functions, such as Dirac algebra simplification, tensor reduction, and loop integration. The square of the amplitude, which is proportional to the probability of the process, is then calculated. This serves as the effective matrix element for the process. This was attempted for the fully hadronic $2 \to 6$ $t\bar{t}$ process. The relatively large amount of particles in the final state made the computation infeasible and was ultimately aborted and the analysis of the angular distributions was performed. In future works, it is possible that the full $2 \to 6$ calculation using the above-mentioned tools can

be achieved with appropriate simplifications that reduce the computational power needed.

7.4.1 Comparing to previous work

The analysis of studying the effects of anomalous couplings by investigating angular distributions done in this thesis overlaps to a large extent with the analysis done in [11], where confidence intervals were determined based on angular distributions of semi-leptonic $t\bar{t}$ pair. The confidence intervals obtained in [11] can be seen in 7.4, where the naming convention is such that ta_ttA is δd_A^γ, tv_ttA is δd_V^γ, vr_ttZ is δX_{tt}^R, tl_tbW_Re is δg_L, tr_tbW_Re is δg_R, vl_tbW_Re is δV_L and vr_tbW_Re is δV_R. In general, the determined sensitivities are in relative agreement. In both cases, the couplings with the highest sensitivities are the couplings where the total cross section is affected the most. The confidence intervals found in this thesis do however, show slightly higher sensitivities. There are a plethora of factors that influence this discrepancy and it is therefore very difficult to know exactly why they differ. In general, the semi-leptonic decay channel has better resolution due the excellent reconstruction of the lepton. However, it also has a slightly lower branching ratio and therefore slightly worse statistics. Additional factors influencing the discrepancy include the event selection as well as the kinematic fit. The kinematic fit is implemented differently with semi-leptonic decays due to the neutrino. Neutrinos are not detected in the detector and are instead inferred from the missing energy, which introduces free parameters in the kinematic fit that are not present with fully hadronic decays where all final state particles are present in the detector.

coupling	σ_{tot}	θ_{et}	θ^*_{tb}	ϕ^*_{tb}	$\theta^*_{W\ell}$	$\phi^*_{W\ell}$
ta_ttA	Yes	-0.08698 to 0.0889	-0.09064 to 0.09425	-0.07231 to 0.07241	-0.05336 to 0.05394	-0.09048 to 0.0941
	No	-0.1599 to 0.1529	-0.7906 to 0.6069	-0.09011 to 0.09155	-0.0552 to 0.05534	-0.2485 to 0.2338
tl_tbW_Re	Yes	-0.1954 to 0.188	-0.1665 to 0.1698	-0.1888 to 0.1781	-0.07797 to 0.07842	-0.1434 to 0.1439
	No	-0.5892 to 0.6208	-0.1969 to 0.215	-0.3068 to 0.2918	-0.07843 to 0.07913	-0.155 to 0.1602
tr_tbW_Re	Yes	-0.001894 to 0.001922	-0.001858 to 0.001884	-0.001732 to 0.001752	-0.001808 to 0.001833	-0.001882 to 0.001909
	No	-0.04373 to 0.05687	-0.01955 to 0.01966	-0.00446 to 0.004435	-0.006526 to 0.006775	-0.02864 to 0.03579
tv_ttA	Yes	-0.0006407 to 0.0006424	-0.0006316 to 0.0006333	-0.0006368 to 0.0006385	-0.0005212 to 0.0005224	-0.0006395 to 0.0006411
	No	-0.01293 to 0.01298	-0.0264 to 0.02269	-0.006161 to 0.006088	-0.0009246 to 0.0009211	-0.008812 to 0.008416
vl_tbW_Re	Yes	-0.003745 to 0.003703	-0.003674 to 0.003631	-0.003576 to 0.003539	-0.002955 to 0.002898	-0.003738 to 0.003694
	No	-0.01547 to 0.01611	-0.0402 to 0.0388	-0.01129 to 0.01152	-0.004909 to 0.004655	-0.03073 to 0.03162
vr_tbW_Re	Yes	-0.3157 to 0.35	-0.3139 to 0.365	-0.1892 to 0.2101	-0.1185 to 0.1258	-0.2361 to 0.204
	No	-0.5007 to 0.4515	-0.4884 to 0.4586	-0.1964 to 0.2127	-0.1193 to 0.1258	-0.2546 to 0.2073
vr_ttZ	Yes	-0.007987 to 0.007884	-0.009419 to 0.009245	-0.008588 to 0.008472	-0.007714 to 0.007477	-0.009588 to 0.009407
	No	-0.01598 to 0.01597	-0.2185 to 0.344	-0.01901 to 0.01925	-0.01362 to 0.01235	-0.1732 to 0.1563

Table 9.3.: Confidence regions for each of the coupling. The first column denotes the name of the coupling, the second column denotes where the information of the cross section was included in the fit and the last columns denotes the confidence interval for the five angles of interest.

Figure 7.4: Confidence intervals found in [11].

8 Conclusion

This thesis focused on exploring the sensitivity to anomalous top couplings in effective field theory, using angular distributions of $t\bar{t}$ pairs in the fully hadronic decay channel.

An event selection process to remove background was implemented with the ROOT software package TMVA. Subsequently, a kinematic fit with constraints was performed in order to reconstruct $t\bar{t}$ pairs as well as determine corrections to measured hadronic jets. The 1σ confidence intervals were determined for each coupling individually by a χ^2 fit to angular distributions based on three different angles. These findings show the potential of the fully hadronic channel for probing new physics.

A comparison to similar work was performed, comparing the sensitivities determined in this thesis to the sensitives determined from semi-leptonic $t\bar{t}$ events. The comparison showed a relatively high degree of agreement, however with most of the couplings having a slightly higher degree of sensitivity in this thesis. Possible reasons for this discrepancy were discussed.

Although this work has successfully determined sensitivities to anomalous couplings, there are still many avenues to be explored. For instance, an analysis combining the different decay modes of the $t\bar{t}$ in order to have a larger event sample and therefore better statistics could be envisioned to improve the confidence intervals of the couplings. As discussed in 7.4, the confidence intervals could also be improved upon by investigating optimal observables, rather than the simple one-dimensional angular distributions that were studied in this thesis.

In conclusion, FCC-ee has the potential of finding small deviations from the Standard Model that could possibly reveal new physics beyond the Standard Model by investigating top quark pairs.

A Event Selection Figures

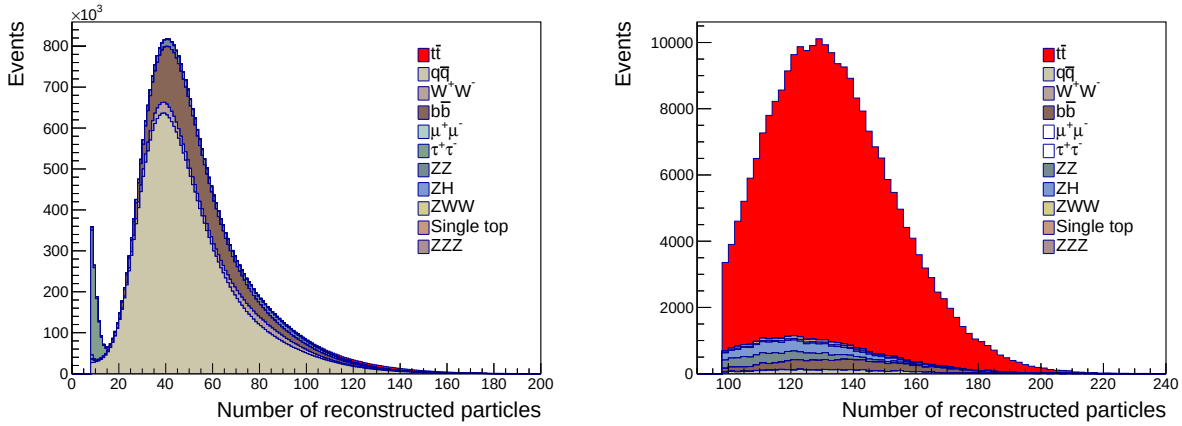

(a) Signal and background prior to cuts.

(b) Selected events after applying cuts.

Figure A.1: Distribution of the number of reconstructed particles before and after applying cuts.

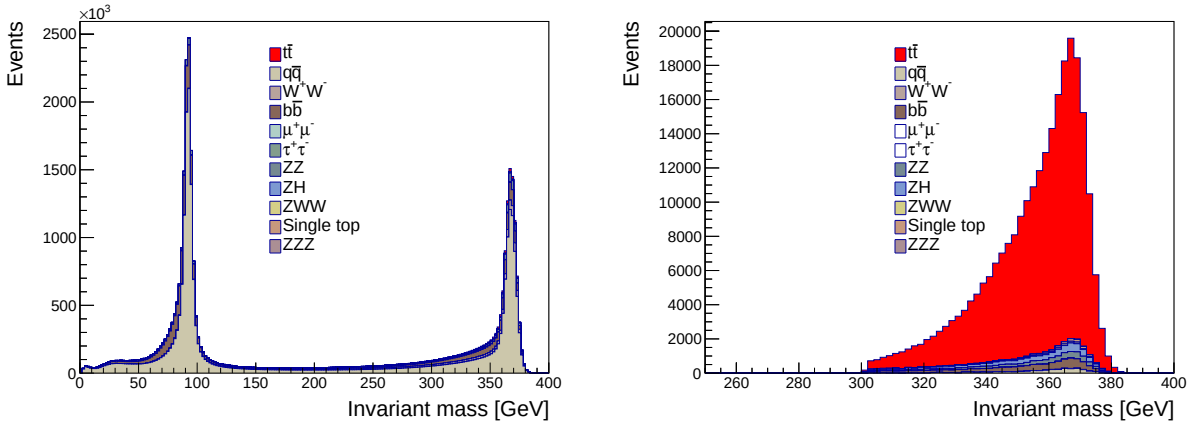

(a) Signal and background prior to cuts.

(b) Selected events after applying cuts.

Figure A.2: Distribution of invariant mass before and after applying cuts.

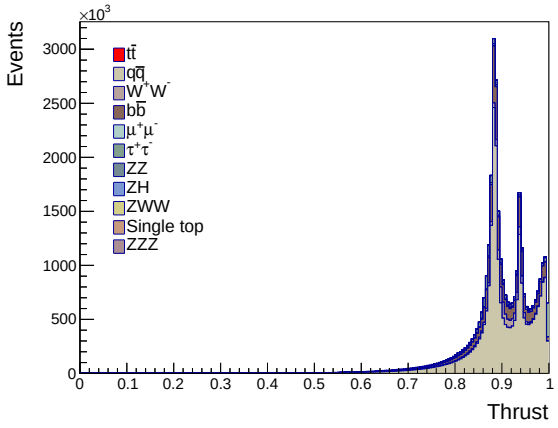

(a) Signal and background prior to cuts.

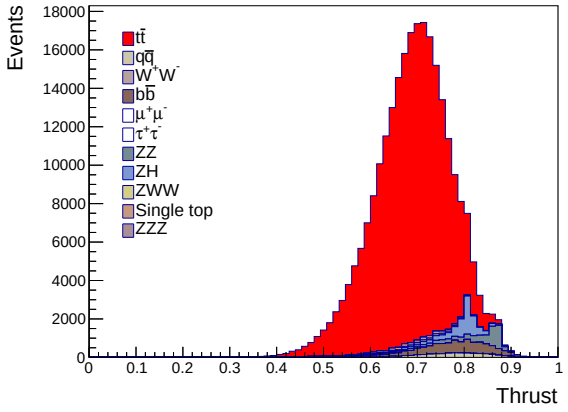

(b) Selected events after applying cuts.

Figure A.3: Distribution of thrust before and after applying cuts.

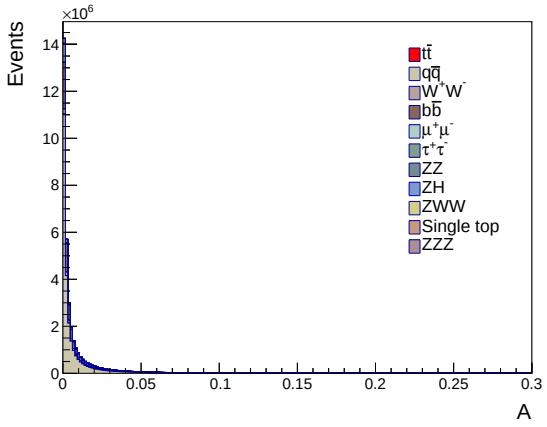

(a) Signal and background prior to cuts.

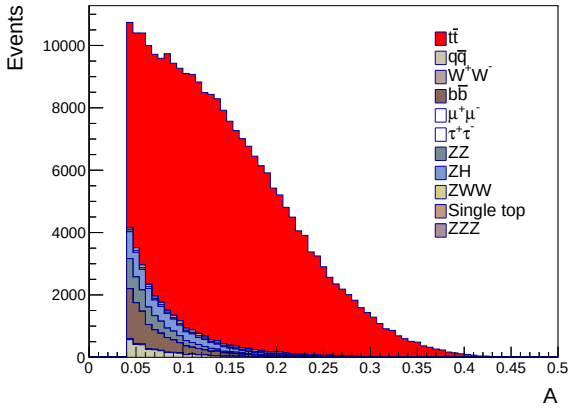

(b) Selected events after applying cuts.

Figure A.4: Distribution of aplanarity before and after applying cuts.

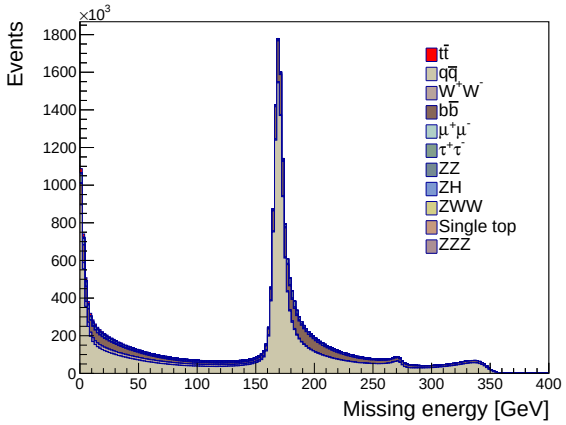

(a) Signal and background prior to cuts.

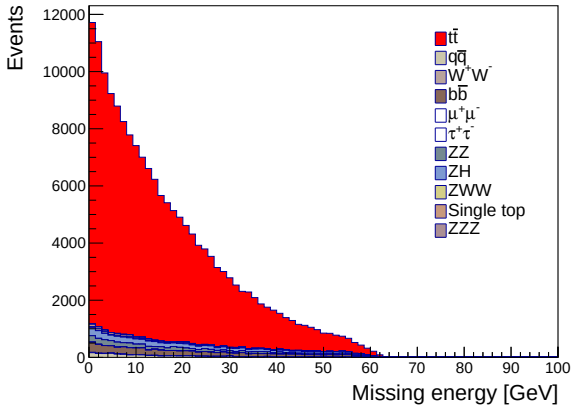

(b) Selected events after applying cuts.

Figure A.5: Distribution of missing energy before and after applying cuts.

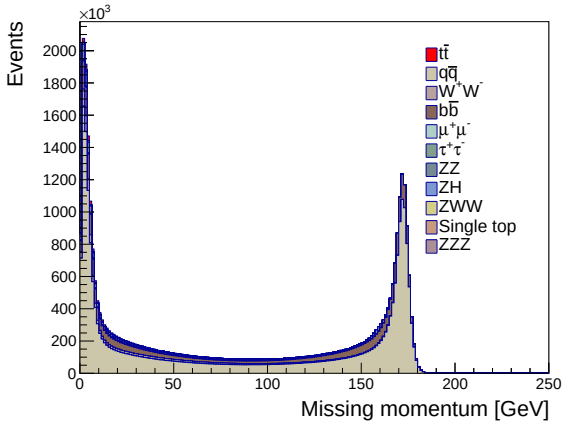

(a) Signal and background prior to cuts.

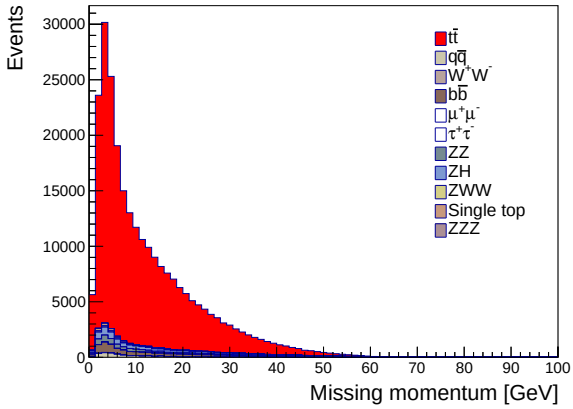

(b) Selected events after applying cuts.

Figure A.6: Distribution of missing momentum before and after applying cuts.

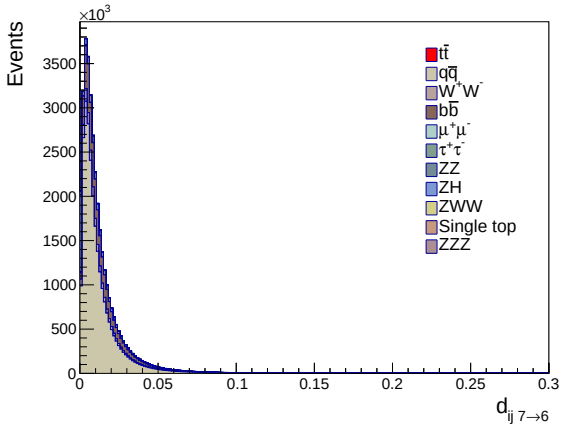

(a) Signal and background prior to cuts.

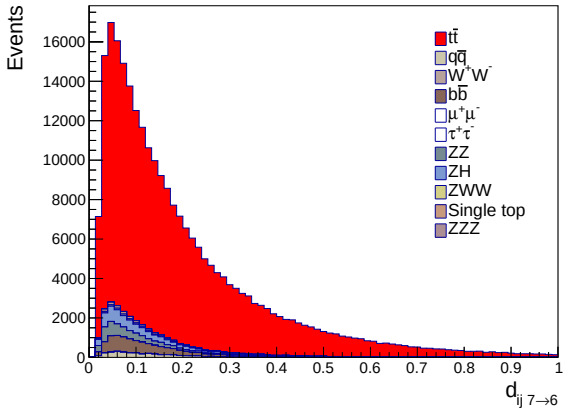

(b) Selected events after applying cuts.

Figure A.7: Distribution of minimum distance measure d_{ij} $7 \rightarrow 6$ before and after applying cuts.

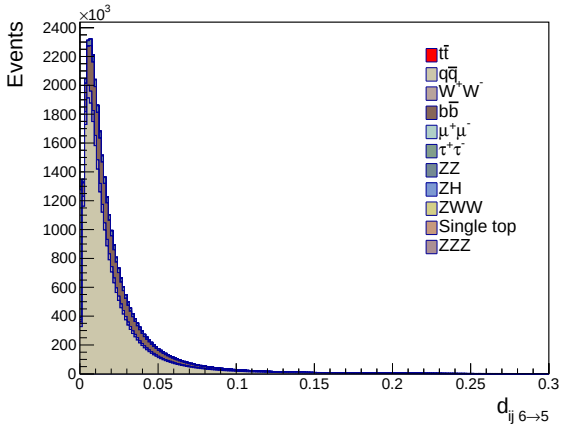

(a) Signal and background prior to cuts.

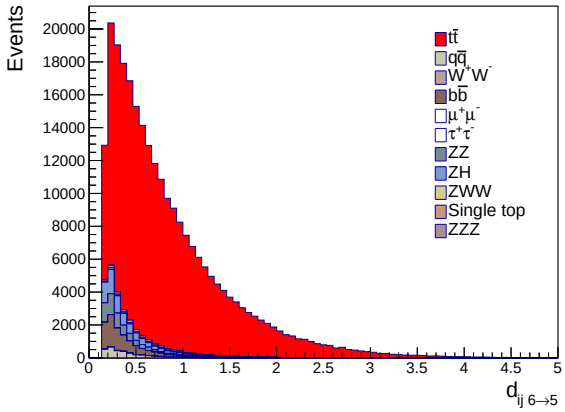

(b) Selected events after applying cuts.

Figure A.8: Distribution of minimum distance measure d_{ij} $6 \rightarrow 5$ before and after applying cuts.

B Results Figures

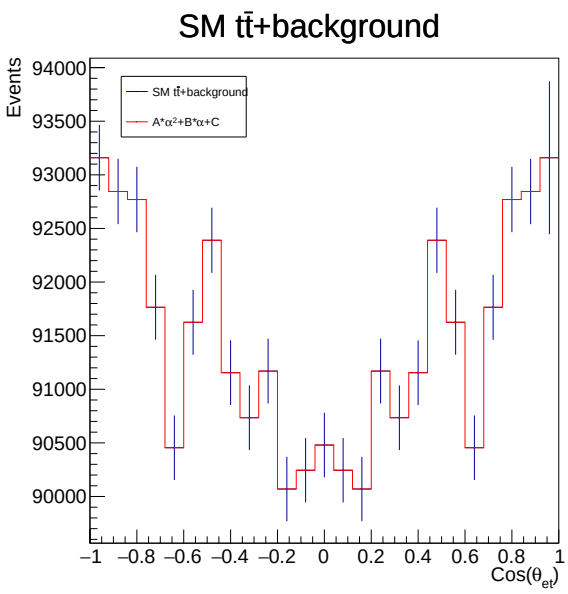

(a) Angular distribution with fit

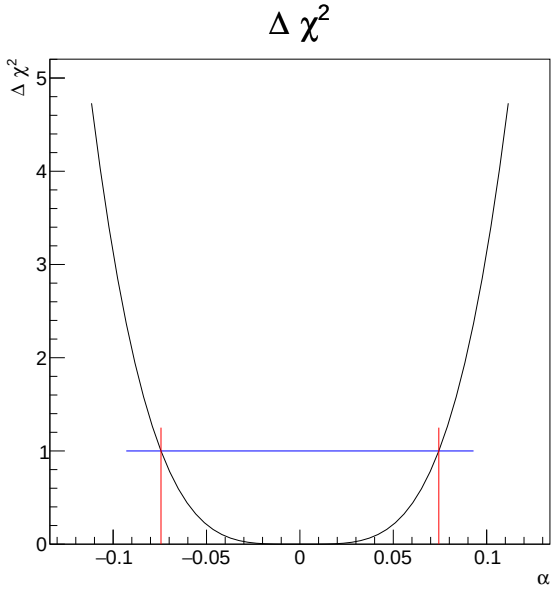

(b) χ^2 distribution and confidence interval

Figure B.1: Angular distribution of $\cos(\theta_{et})$ and χ^2 distribution of coupling δV_L.

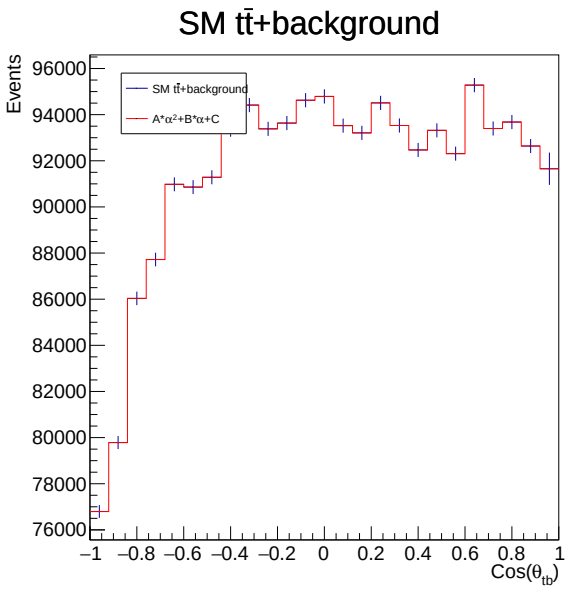

(a) Angular distribution with fit

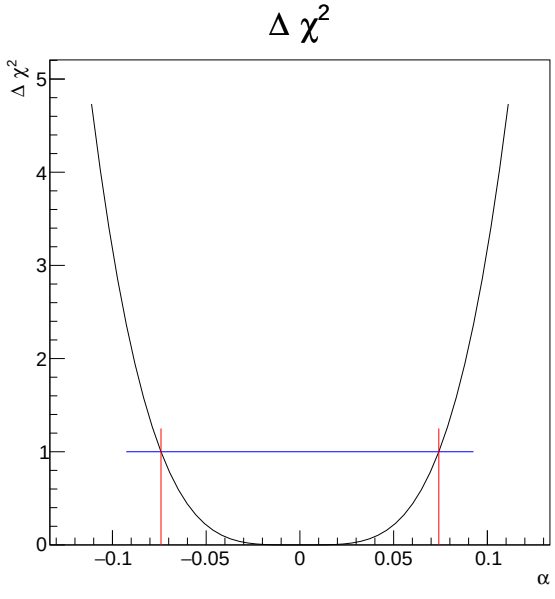

(b) χ^2 distribution and confidence interval

Figure B.2: Angular distribution of $\cos(\theta_{tb})$ and χ^2 distribution of coupling δV_L.

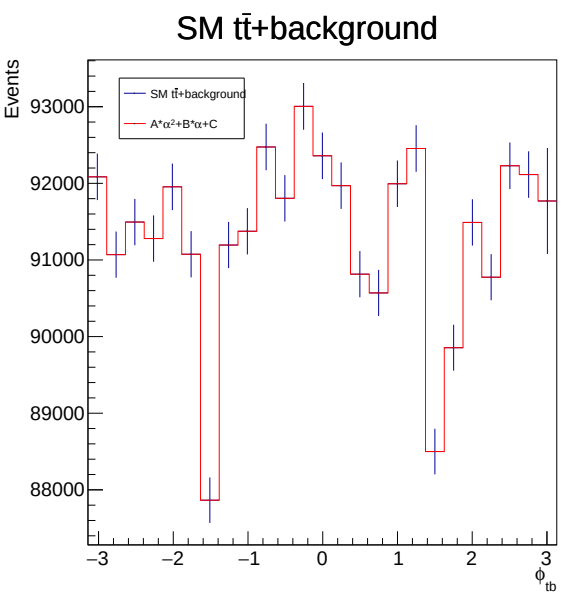

(a) Angular distribution with fit

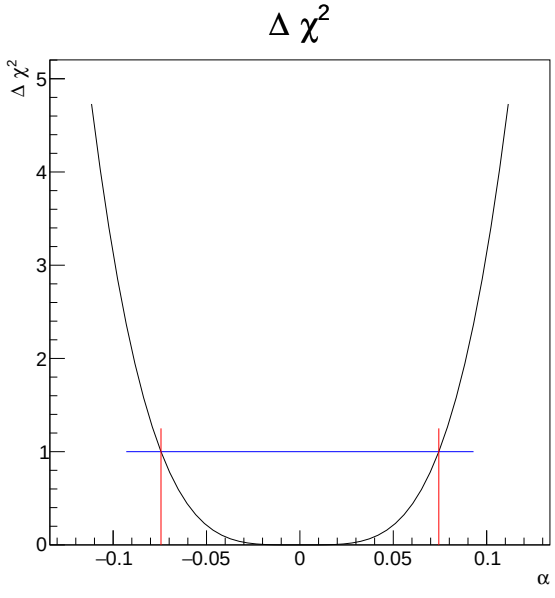

(b) χ^2 distribution and confidence interval

Figure B.3: Angular distribution of ϕ_{tb} and χ^2 distribution of coupling δV_L.

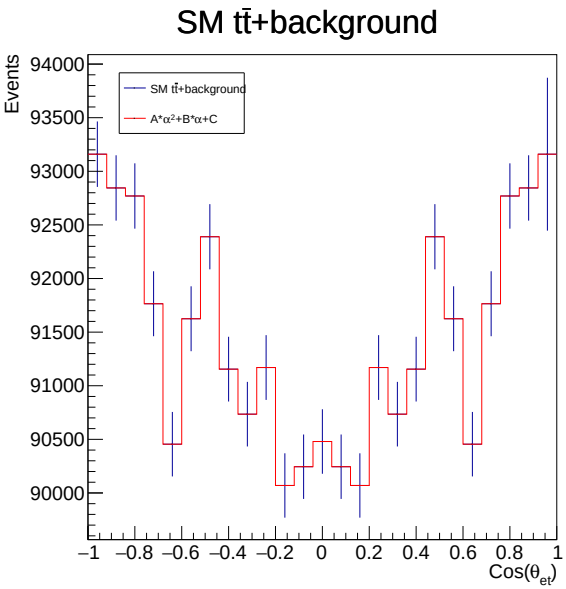

(a) Angular distribution with fit

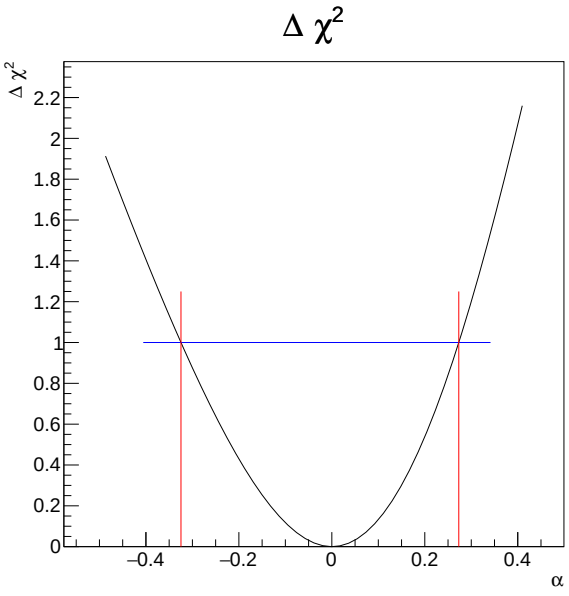

(b) χ^2 distribution and confidence interval

Figure B.4: Angular distribution of $\cos(\theta_{et})$ and χ^2 distribution of coupling δV_R.

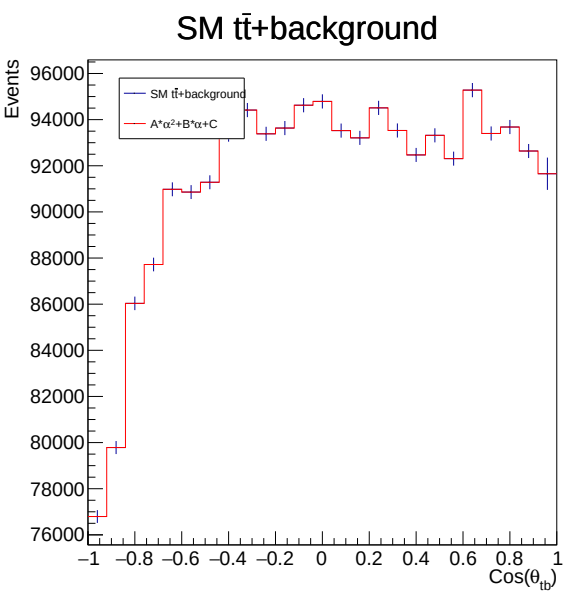

(a) Angular distribution with fit

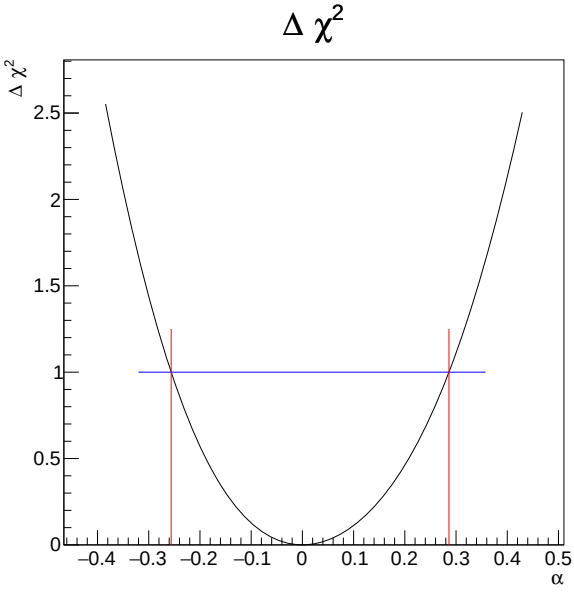

(b) χ^2 distribution and confidence interval

Figure B.5: Angular distribution of $\cos(\theta_{tb})$ and χ^2 distribution of coupling δV_R.

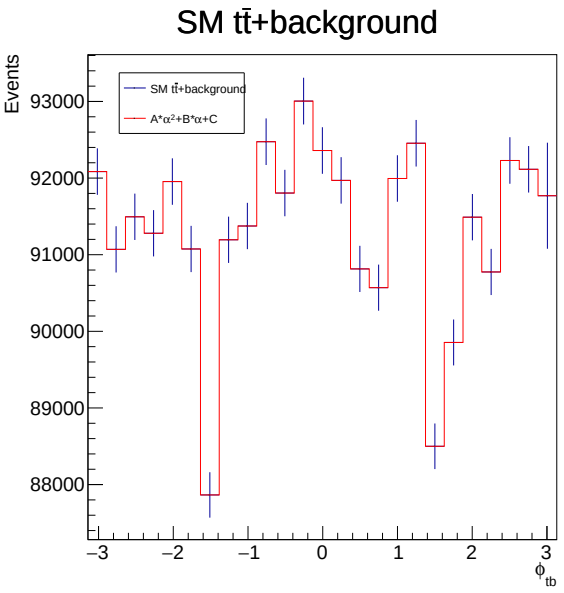

(a) Angular distribution with fit

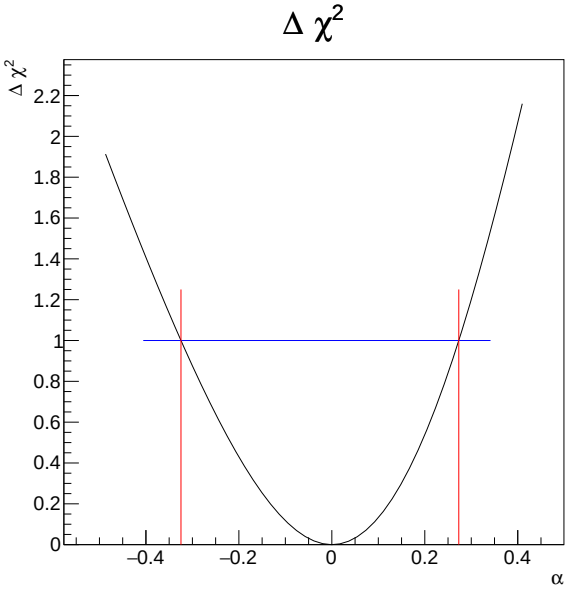

(b) χ^2 distribution and confidence interval

Figure B.6: Angular distribution of ϕ_{tb} and χ^2 distribution of coupling δV_R.

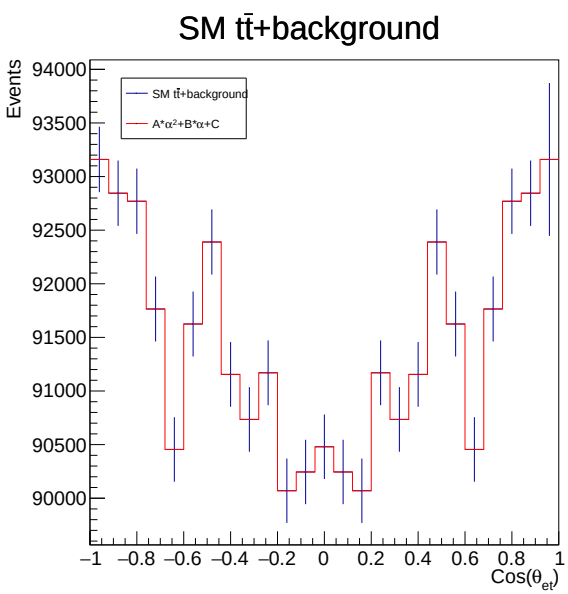

(a) Angular distribution with fit

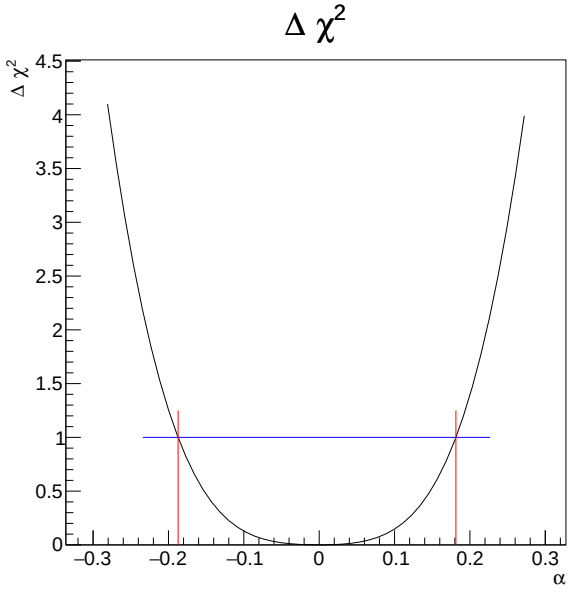

(b) χ^2 distribution and confidence interval

Figure B.7: Angular distribution of $\cos(\theta_{et})$ and χ^2 distribution of coupling δg_L.

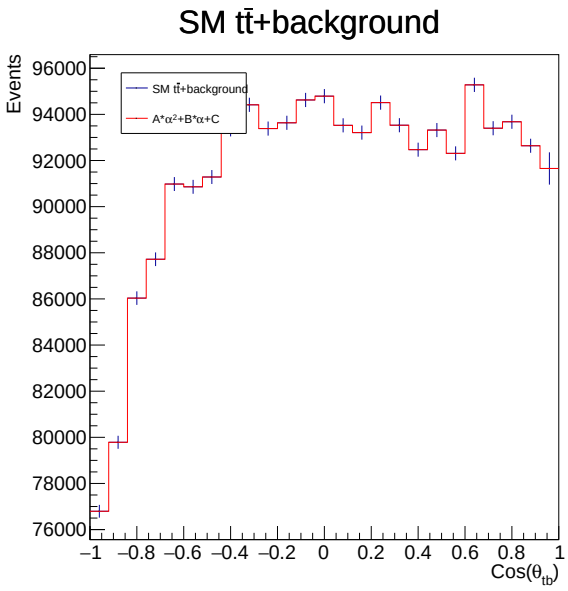

(a) Angular distribution with fit

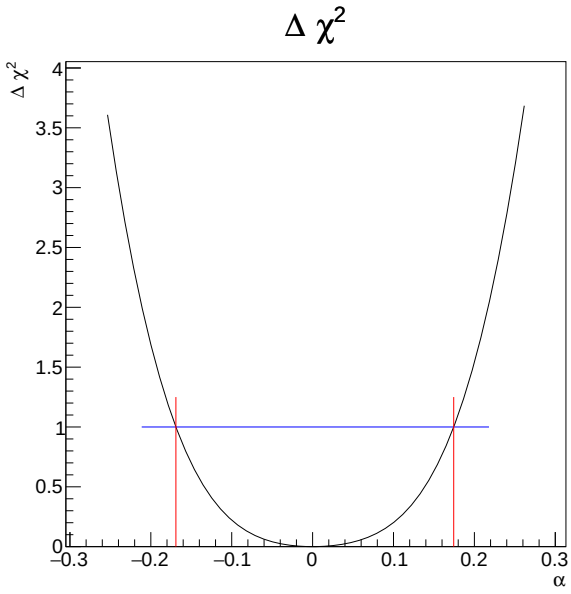

(b) χ^2 distribution and confidence interval

Figure B.8: Angular distribution of $\cos(\theta_{tb})$ and χ^2 distribution of coupling δg_L.

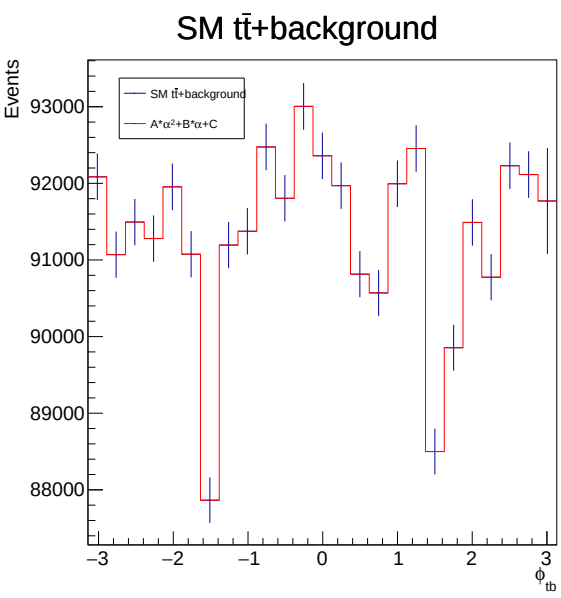

(a) Angular distribution with fit

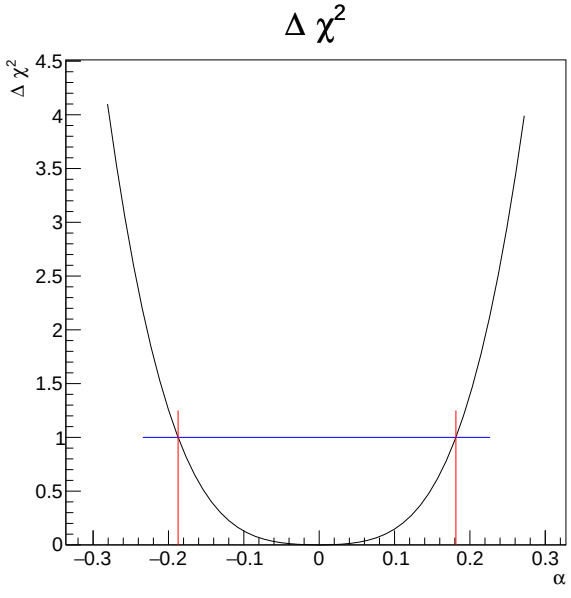

(b) χ^2 distribution and confidence interval

Figure B.9: Angular distribution of ϕ_{tb} and χ^2 distribution of coupling δg_L.

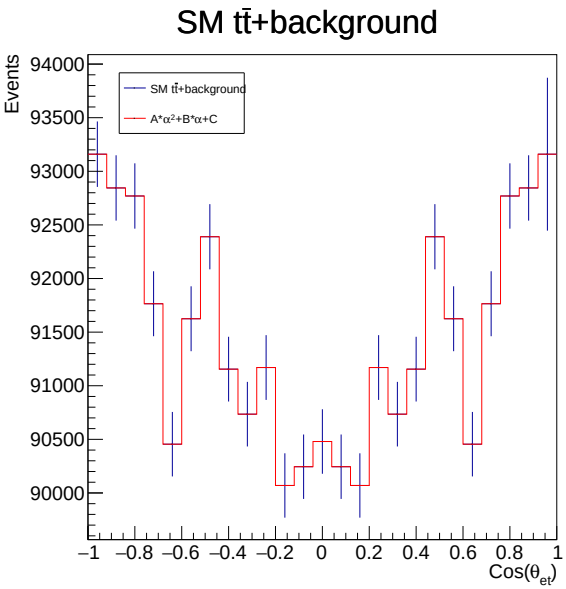

(a) Angular distribution with fit

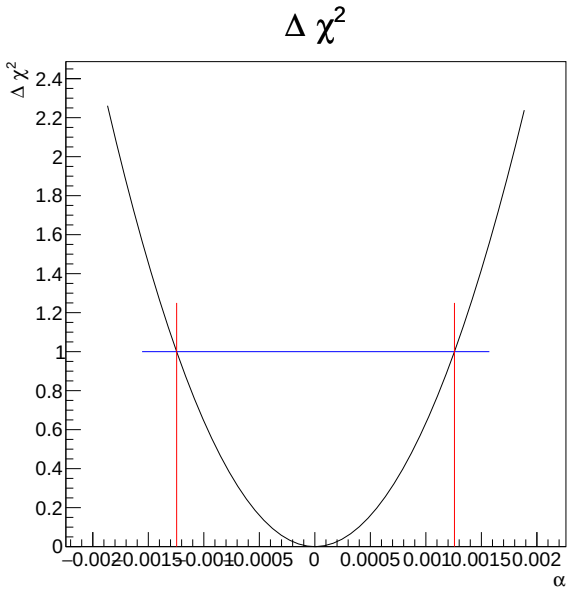

(b) χ^2 distribution and confidence interval

Figure B.10: Angular distribution of $\cos(\theta_{et})$ and χ^2 distribution of coupling δg_R.

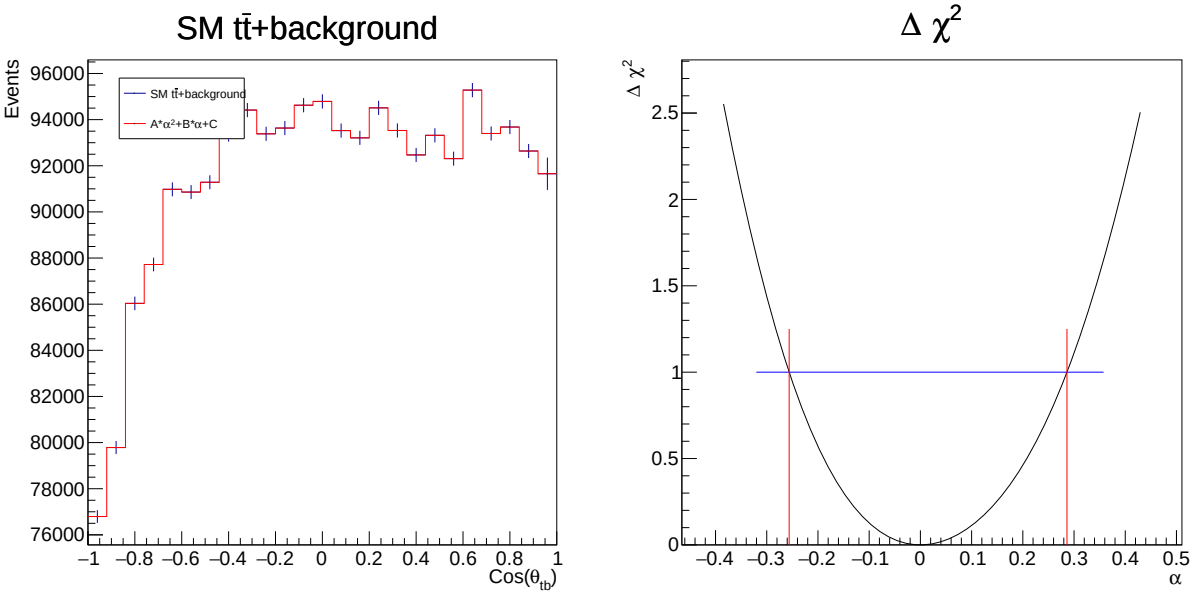

(a) Angular distribution with fit (b) χ^2 distribution and confidence interval

Figure B.11: Angular distribution of $\cos(\theta_{tb})$ and χ^2 distribution of coupling δg_R.

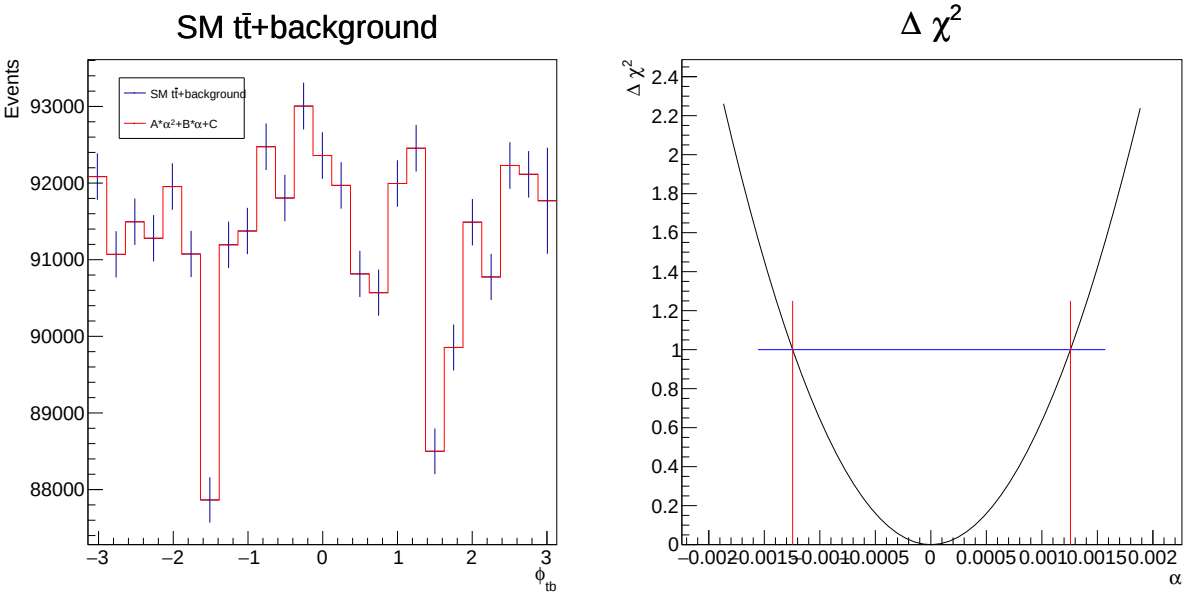

(a) Angular distribution with fit (b) χ^2 distribution and confidence interval

Figure B.12: Angular distribution of ϕ_{tb} and χ^2 distribution of coupling δg_R.

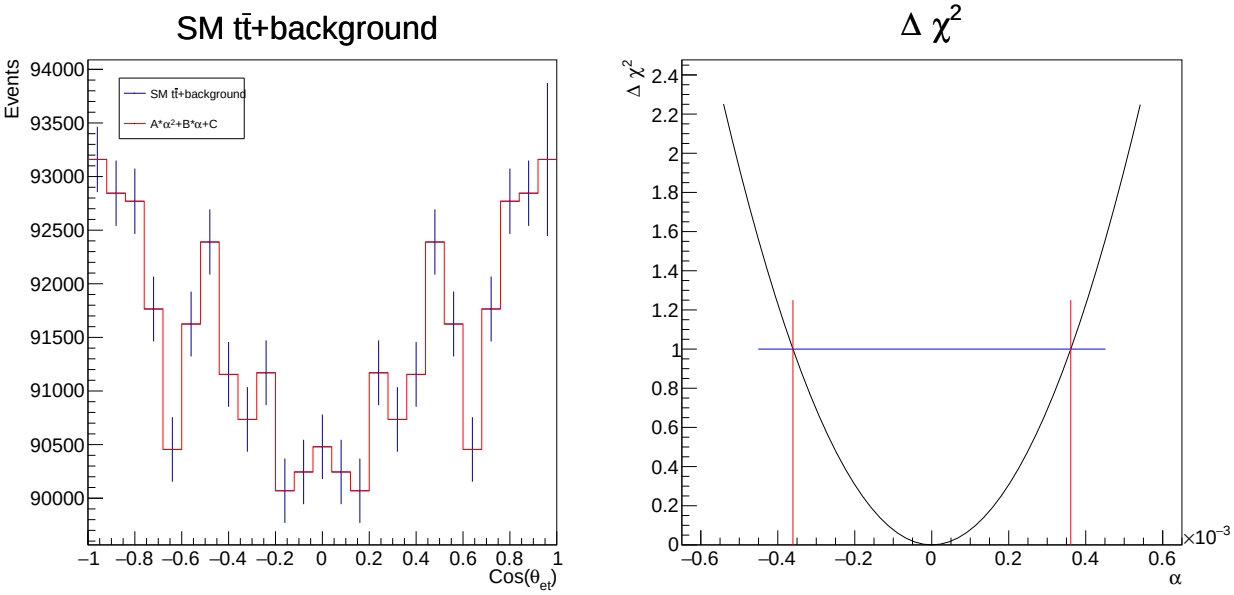

(a) Angular distribution with fit (b) χ^2 distribution and confidence interval

Figure B.13: Angular distribution of $\cos(\theta_{et})$ and χ^2 distribution of coupling δd_V^γ.

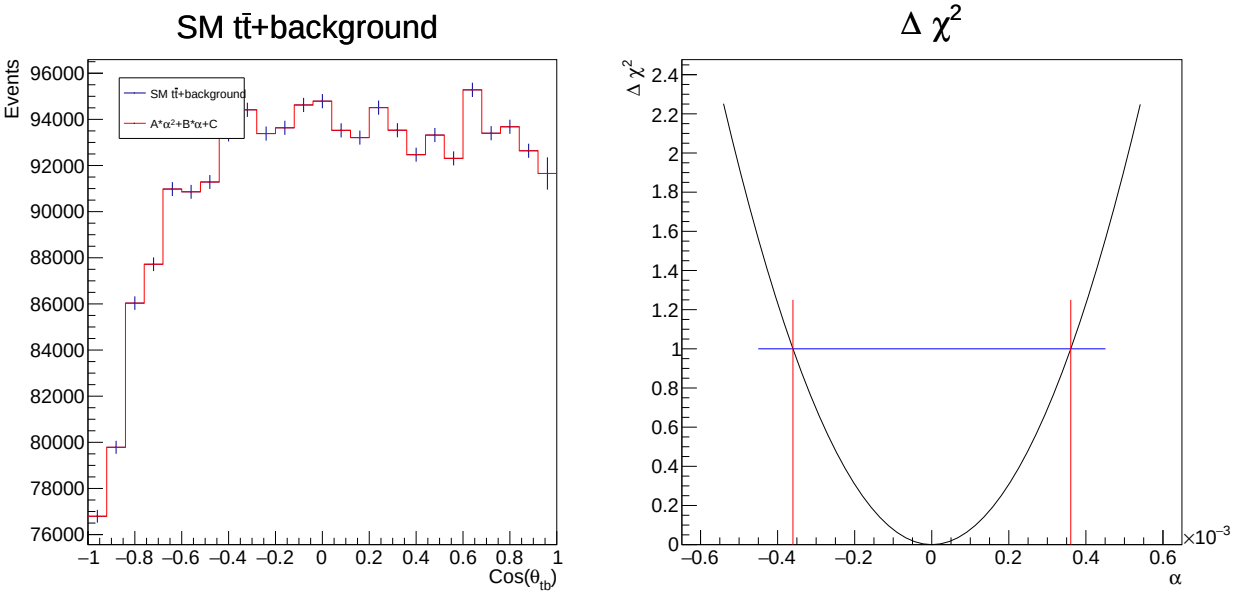

(a) Angular distribution with fit (b) χ^2 distribution and confidence interval

Figure B.14: Angular distribution of $\cos(\theta_{tb})$ and χ^2 distribution of coupling δd_V^γ.

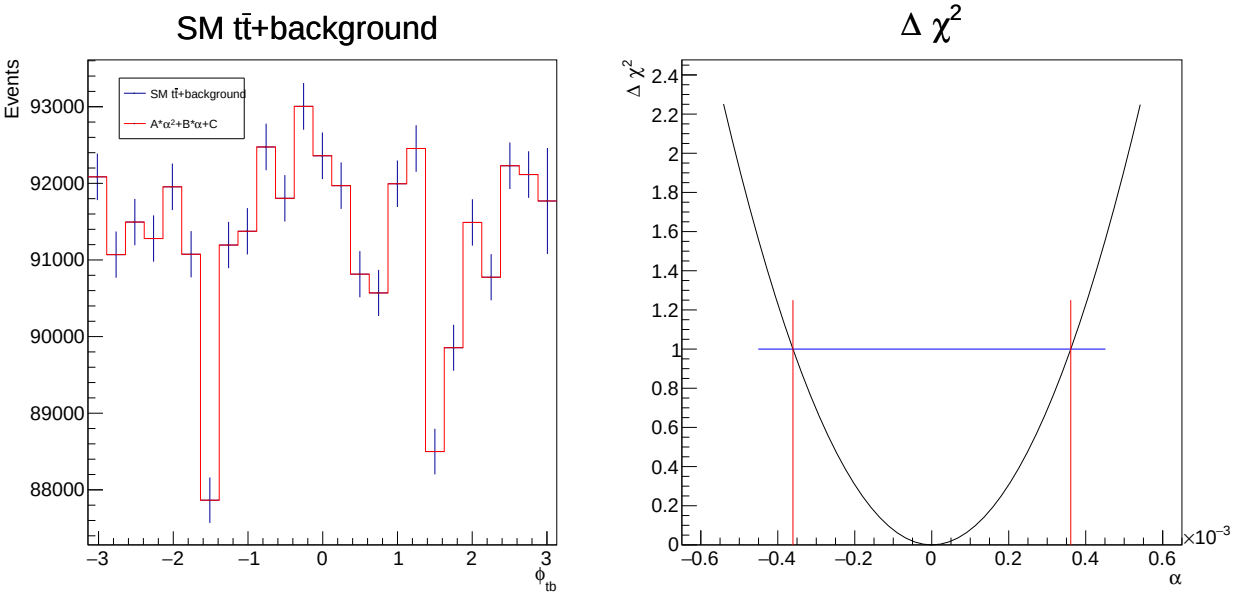

(a) Angular distribution with fit (b) χ^2 distribution and confidence interval

Figure B.15: Angular distribution of ϕ_{tb} and χ^2 distribution of coupling δd_V^γ.

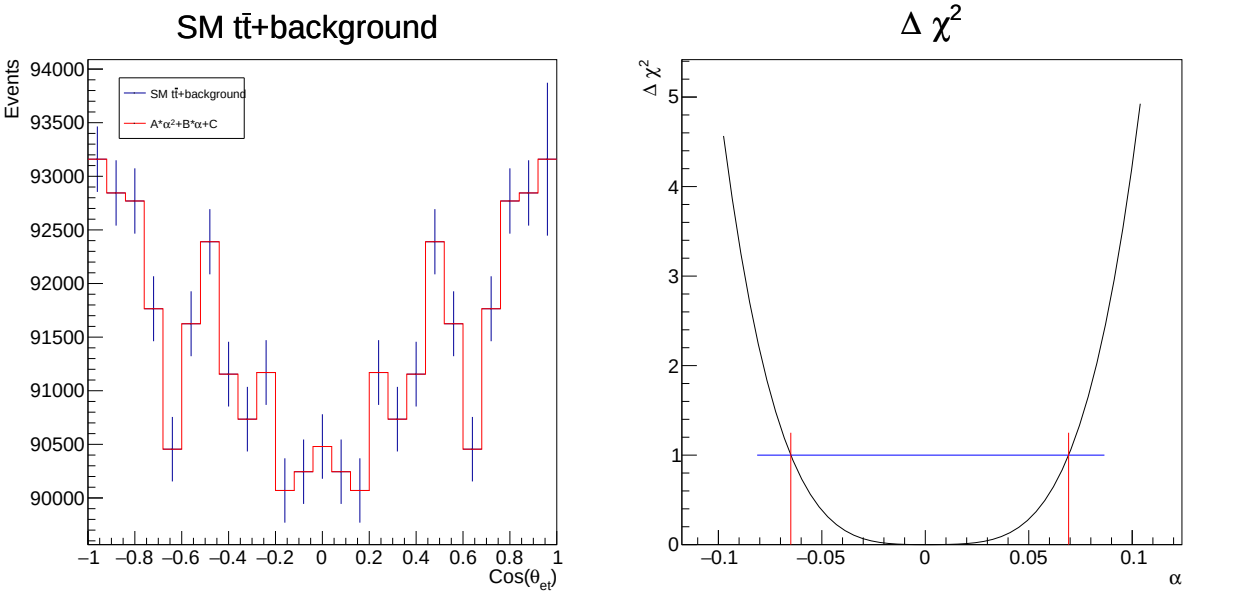

(a) Angular distribution with fit (b) χ^2 distribution and confidence interval

Figure B.16: Angular distribution of $\cos(\theta_{et})$ and χ^2 distribution of coupling δd_A^γ.

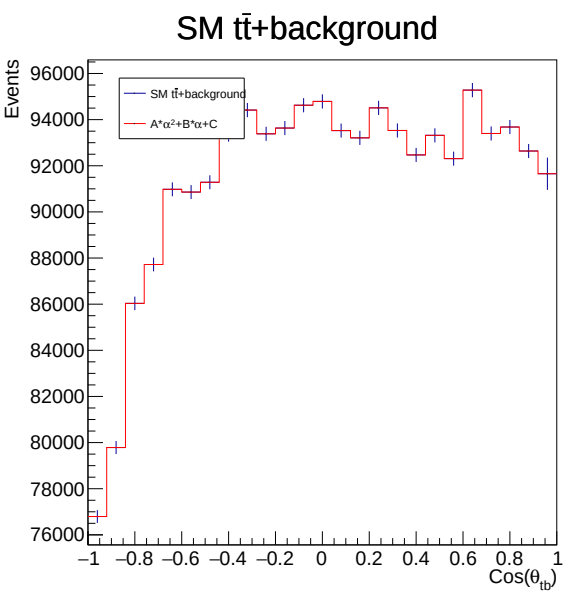

(a) Angular distribution with fit

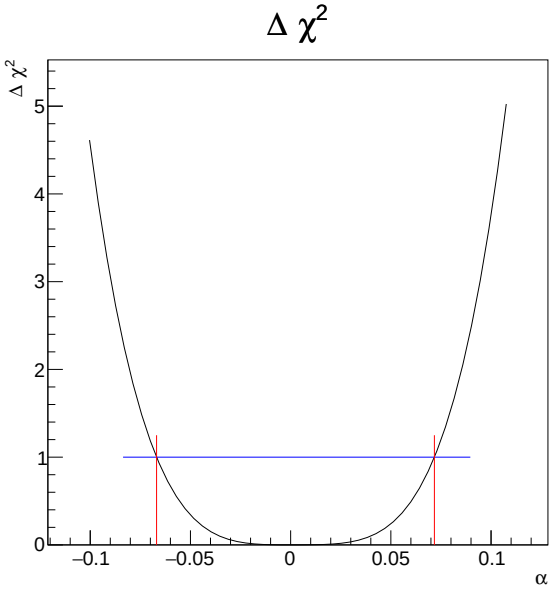

(b) χ^2 distribution and confidence interval

Figure B.17: Angular distribution of $\cos(\theta_{tb})$ and χ^2 distribution of coupling δd_A^γ.

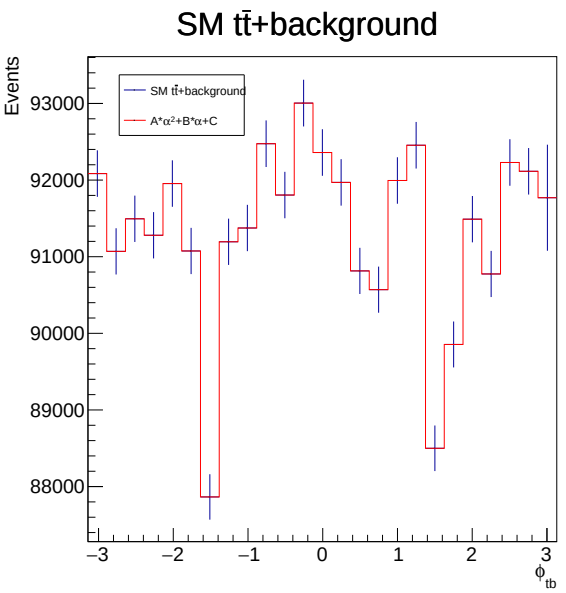

(a) Angular distribution with fit

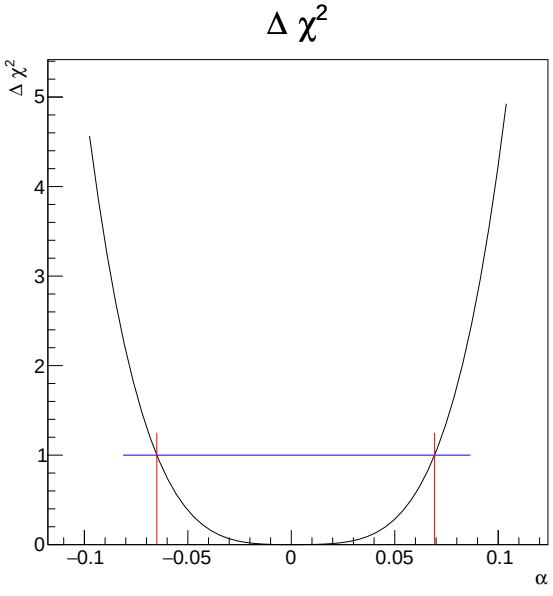

(b) χ^2 distribution and confidence interval

Figure B.18: Angular distribution of ϕ_{tb} and χ^2 distribution of coupling δd_A^γ.

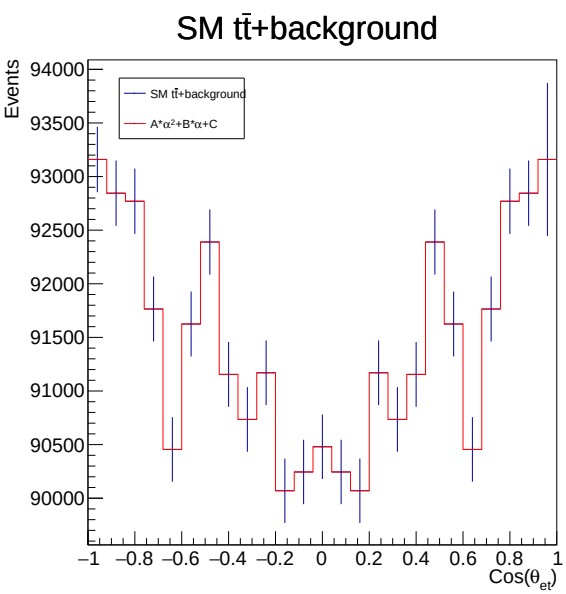

(a) Angular distribution with fit

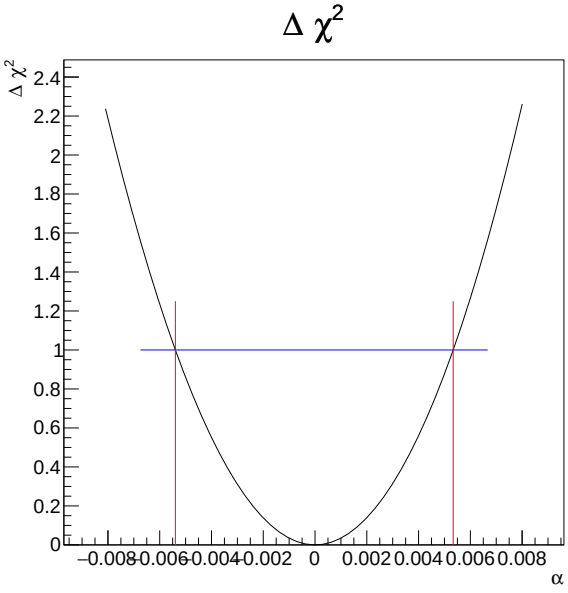

(b) χ^2 distribution and confidence interval

Figure B.19: Angular distribution of $\cos(\theta_{et})$ and χ^2 distribution of coupling δX_{tt}^R.

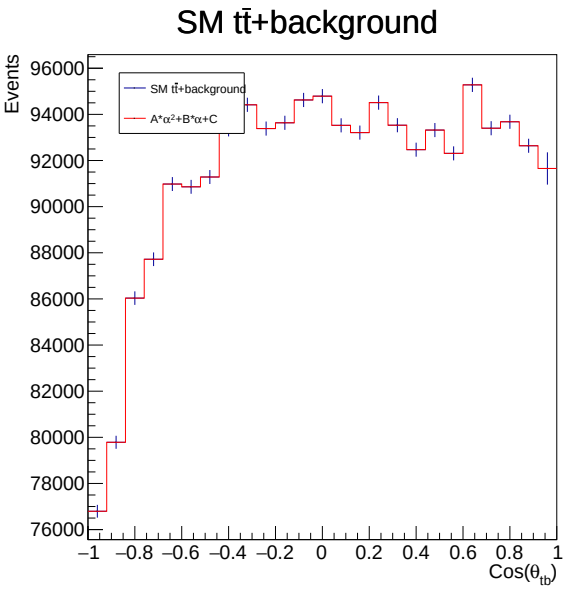

(a) Angular distribution with fit

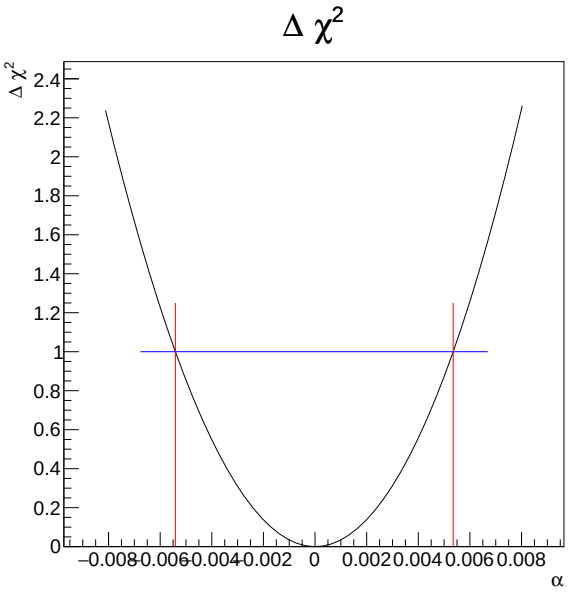

(b) χ^2 distribution and confidence interval

Figure B.20: Angular distribution of $\cos(\theta_{tb})$ and χ^2 distribution of coupling δX_{tt}^R.

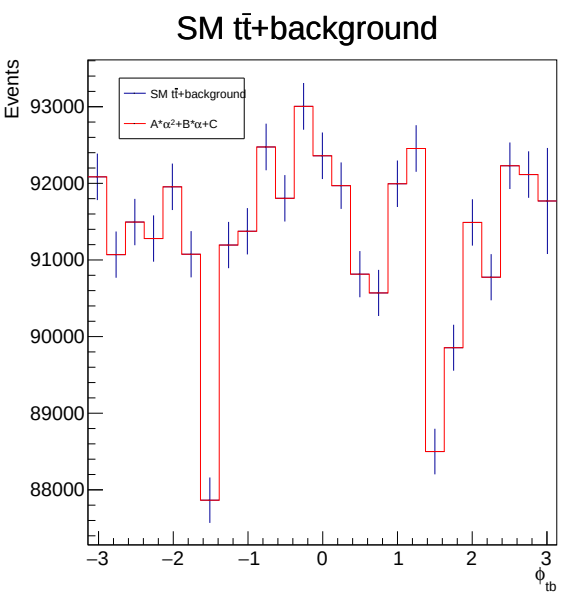

(a) Angular distribution with fit

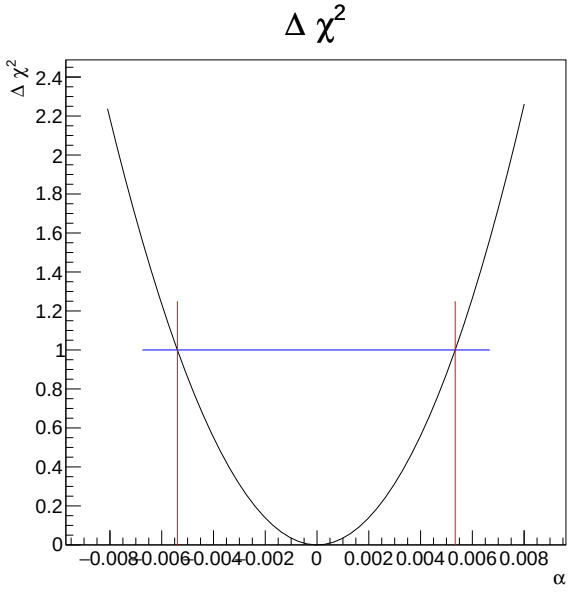

(b) χ^2 distribution and confidence interval

Figure B.21: Angular distribution of ϕ_{tb} and χ^2 distribution of coupling δX_{tt}^R.

List of Figures

List of Tables

C References

[1] Mark Thomson. *Modern Particle Physics*. Cambridge University Press, 2013.

[2] J. A. Aguilar-Saavedra. A Minimal set of top anomalous couplings. *Nucl. Phys. B*, 812:181–204, 2009.

[3] Fabiola Gianotti. CERN Vision and Plans. `https://indico.bnl.gov/event/18372/contributions/75206/attachments/47011/79716/CERN-plans.pdf`, April 13 2023.

[4] The FCC Collaboration. *FCC-ee: The Lepton Collider Future Circular Collider Conceptual Design Report Volume 2*. The European Physical Journal Special Topics 228, 2019.

[5] Valentin Volk et al. FCCSW. `https://github.com/HEP-FCC`, 2023.

[6] Torbjörn Sjöstrand et al. A comprehensive guide to the physics and usage of PYTHIA 8.3. *SciPost Phys. Codebases 8 (2022)*, 3 2022.

[7] J. de Favereau, C. Delaere, P. Demin, A. Giammanco, V. Lemaître, A. Mertens, and M. Selvaggi. DELPHES 3, A modular framework for fast simulation of a generic collider experiment. *JHEP*, 02:057, 2014.

[8] EDM4hep. Github. `https://github.com/key4hep/EDM4hep`.

[9] R. Brun and F. Rademakers. ROOT: An object oriented data analysis framework. *Nucl. Instrum. Meth. A*, 389:81–86, 1997.

[10] M. Z. Akrawy et al. A Study of the recombination scheme dependence of jet production rates and of alpha-s (m(Z0)) in hadronic Z0 decays. *Z. Phys. C*, 49:375–384, 1991.

[11] Julie M. Torndal. A Study of Top Anomalous Couplings at a Future e+e- Collider. *Master's thesis*, 2021.

[12] Matteo Cacciari, Gavin P. Salam, and Gregory Soyez. FastJet User Manual. *Eur. Phys. J. C*, 72:1896, 2012.

[13] R. L. Workman et al. Review of Particle Physics. *PTEP*, 2022:083C01, 2022.

[14] J. Alwall, R. Frederix, S. Frixione, V. Hirschi, F. Maltoni, O. Mattelaer, H. S. Shao, T. Stelzer, P. Torrielli, and M. Zaro. The automated computation of tree-level and next-to-leading order differential cross sections, and their matching to parton shower simulations. *JHEP*, 07:079, 2014.

[15] Wolfgang Kilian, Thorsten Ohl, and Jurgen Reuter. WHIZARD: Simulating Multi-Particle Processes at LHC and ILC. *Eur. Phys. J. C*, 71:1742, 2011.

[16] Jan Therhaag. TMVA Toolkit for multivariate data analysis in ROOT. *PoS*, ICHEP2010:510, 2010.

[17] Andreas Hoecker. Multivariate Data Analysis with TMVA. https://indico.desy.de/event/1097/contributions/3636/attachments/2596/2977/TMVA_DESYStatWS_19jun08_hoecker.pdf, June 19 2008.

[18] Volker Blobel. Least squares methods. http://graduierten-kurse.physi.uni-heidelberg.de/WiSe2003/lectures/blobel/export/lsqu/master.pdf, October 2003.

[19] Julie Munch Torndal and Jørgen Beck Hansen. ABCfit++. https://github.com/Torndal/ABCfitplusplus, 2021.

[20] Niels Vestergaard. Phenomenological study of anomalous $t\bar{t}$ production at FCC-ee. *Bachelor thesis*, 2021.

[21] M. Diehl and O. Nachtmann. Optimal observables for the measurement of three gauge boson couplings in e+ e- —> W+ W-. *Z. Phys. C*, 62:397–412, 1994.

[22] R. Mertig and J. Kublbeck. Feyn Arts and Feyn Calc: Computeralgebraic generation and calculation of Feynman diagrams for radiative corrections. In *International Workshop on Software Engineering, Artificial Intelligence and Expert Systems for High-energy and Nuclear Physics*, pages 565–572, 3 1990.

[23] Wolfram Research, Inc. Mathematica, Version 13.2. Champaign, IL, 2022.

[24] Adam Alloul, Neil D. Christensen, Céline Degrande, Claude Duhr, and Benjamin Fuks. FeynRules 2.0 - A complete toolbox for tree-level phenomenology. *Comput. Phys. Commun.*, 185:2250–2300, 2014.